JGR Atmospheres

RESEARCH ARTICLE
10.1029/2021JD035810

Influence of Large-Scale Atmospheric Dynamics on Precipitation Seasonality of the Tibetan Plateau and Central Asia in Cold and Warm Climates During the Late Cenozoic

Svetlana Botsyun[1,2], Sebastian G. Mutz[1], Todd A. Ehlers[1], Alexander Koptev[1,3], Xun Wang[4], Benjamin Schmidt[4], Erwin Appel[1], and Dieter E. Scherer[4]

[1]Department of Geosciences, University of Tübingen, Tübingen, Germany, [2]Institute of Meteorology, Freie Universität Berlin, Berlin, Germany, [3]Helmholtz Centre Potsdam, GFZ German Research Centre for Geosciences, Potsdam, Germany, [4]Chair of Climatology, Technische Universität Berlin, Berlin, Germany

Key Points:

- High-resolution general circulation model (ECHAM5) is used to study past changes in hydroclimate in the Tibetan Plateau and Central Asia
- Seasons with high precipitation rates were longer in the mid-Pliocene and shorter in the Last Glacial Maximum compared to the pre-industrial
- Late Cenozoic hydroclimate of the region is linked to the dynamics of the mid-latitude jet stream and the Indo-Asian monsoon circulation

Supporting Information:

Supporting Information may be found in the online version of this article.

Correspondence to:

S. Botsyun,
svetlana.botsyun@fu-berlin.de

Citation:

Botsyun, S., Mutz, S. G., Ehlers, T. A., Koptev, A., Wang, X., Schmidt, B., et al. (2022). Influence of large-scale atmospheric dynamics on precipitation seasonality of the Tibetan Plateau and Central Asia in cold and warm climates during the Late Cenozoic. *Journal of Geophysical Research: Atmospheres*, *127*, e2021JD035810. https://doi.org/10.1029/2021JD035810

Received 4 SEP 2021
Accepted 18 MAY 2022

Author Contributions:

Conceptualization: Svetlana Botsyun, Sebastian G. Mutz, Todd A. Ehlers, Erwin Appel, Dieter E. Scherer
Data curation: Svetlana Botsyun
Formal analysis: Svetlana Botsyun
Funding acquisition: Sebastian G. Mutz, Todd A. Ehlers, Erwin Appel, Dieter E. Scherer
Investigation: Svetlana Botsyun, Alexander Koptev

Abstract The hydroclimate of the Tibetan Plateau (TP) and Central Asia (CA) plays a crucial role in sustaining surface water reservoirs and thus water resources in the respective regions. In this study, we investigate the changes in Asian hydroclimate and its driving forces during specific time intervals in the last 3 Ma. We conduct high-resolution (~0.75° per grid cell) general circulation model ECHAM-5 experiments with boundary conditions for the mid-Pliocene (~3 Ma), the Last Glacial Maximum (LGM; ~21 ka), the mid-Holocene (~6 ka), and the pre-industrial. Results suggest that seasonally relatively high precipitation rates (>1 mm day^{-1}) were longer in the mid-Pliocene and shorter in the LGM, relative to the pre-industrial. We calculate different monsoon indices to detect changes in the intensity, strength and duration of the East Asian summer monsoon (EASM), South Asian summer monsoon (SASM), and the Indian summer monsoon (ISM), and construct climatologies of mid-latitude high-level westerly jet (WJ) stream occurrences based on the ECHAM5 wind fields. Our results suggest that in warm periods (e.g., mid-Pliocene or interglacial), the WJ migrates northward earlier in the year (April) and reaches higher latitudes than in the pre-industrial, resulting in a wetter TP and CA. During cooler periods (e.g., LGM or glacial), the WJ migrates northward later in the year (June) and remains over lower latitudes, resulting in a drier TP and CA. Increased/decreased local precipitation in TP and CA for the mid-Pliocene/LGM experiments correlates strongly with (a) intensity, strength and duration of the EASM, SASM, and the ISM and (b) WJ latitudinal position.

1. Introduction

The present-day spatial and temporal variability of precipitation over the Tibetan Plateau (TP) and Central Asia (CA) are complex and involve different physical mechanisms (Bohner, 2006; Bothe et al., 2012; Mölg et al., 2014). General circulation models (GCMs) and high-resolution reanalysis datasets provide the necessary tools to explain past and present-day observed precipitation patterns (Botsyun et al., 2019; Knorr et al., 2011; Li, Ehlers, Werner, et al., 2016; Licht et al., 2014; Maussion et al., 2014; Mölg et al., 2014; Mutz et al., 2018; Saeed et al., 2011; Wang, Tolksdorf, et al., 2021). Temporal changes in hydroclimate across the TP and CA regions during the Late Cenozoic are driven by both thermodynamic and dynamic processes (Caves et al., 2014; Han et al., 2021; Li & Morrill, 2010, 2013; Sun, Wu, Ramstein, et al., 2021). An important thermodynamic effect arises from two factors: first, a change in the specific humidity gradient caused by reduced/increased evaporation over the ocean during colder/warmer periods (e.g., Jin et al., 2012); second, an enhanced land-sea thermal contrast (Joshi et al., 2008). Regional changes in atmospheric dynamics and associated changes in moisture advection are related to the shift in pressure gradients and the latitudinal tilt of the westerly winds (Li & Morrill, 2013; Lü et al., 2010) or different influences of Indian summer monsoon (ISM), South Asian summer monsoon (SASM), and East Asian summer monsoon (EASM) (Wang et al., 2003).

Previous studies have shown that the present-day moisture supply to the Tian Shan region, the Tarim Basin, adjacent regions of Kyrgyzstan and Kazakhstan, Northwestern China and the northern TP is primarily controlled by mid-latitude westerlies, and also from contributions from higher latitudes (Bothe et al., 2012). The ISM, SASM, and EASM also have an influence on the regional hydroclimate through advection of moisture from the Indian and Pacific Oceans. Their contributions range from 20% to 45% (depending of region and season) of the total moisture reaching the TP and CA (Botsyun et al., 2016; Jiang et al., 2020; Pan et al., 2019; Yao et al., 2013). Moreover, the monsoon circulation has a strong dynamic link with precipitation in this region through the

Methodology: Svetlana Botsyun, Sebastian G. Mutz, Alexander Koptev, Dieter E. Scherer
Resources: Sebastian G. Mutz
Software: Svetlana Botsyun, Alexander Koptev
Supervision: Todd A. Ehlers
Validation: Sebastian G. Mutz, Todd A. Ehlers, Alexander Koptev, Xun Wang, Benjamin Schmidt, Erwin Appel, Dieter E. Scherer
Visualization: Svetlana Botsyun, Alexander Koptev
Writing – original draft: Svetlana Botsyun
Writing – review & editing: Sebastian G. Mutz, Todd A. Ehlers, Alexander Koptev, Xun Wang, Benjamin Schmidt, Erwin Appel, Dieter E. Scherer

so-called "monsoon-desert" coupling mechanism. The monsoon-desert mechanism results from diabatic heating in the monsoon region that induces Rossby waves which interact with subtropical westerly flows and causes a descending motion north of the TP (Hoskins, 1996). This dry air subsidence north of the TP and associated dryness of CA increases with a strengthened summer monsoon (Broccoli & Manabe, 1992).

For the present-day climate, precipitation conditions over the central TP in May-June are largely determined by both the onset of the ISM and mid-latitude dynamics (Mölg et al., 2014). Moreover, strong coupling between the westerly jet (WJ) stream and lower-level circulation (Wu, Liu, et al., 2012) and between atmospheric moisture transport and local precipitation (Ma et al., 2018) have been hypothesized for the Asian region. Mölg et al. (2014) showed that (a) WJ suppresses deep convection through vertical wind shear in the upper troposphere and thus reduces regional precipitation, and (b) WJ induces atmospheric moisture fluxes in the lower to mid-troposphere. Furthermore, large-scale westerly waves remotely control the tropospheric flow strength over the TP (Mölg et al., 2014). In turn, the latitudinal position and occurrence of the WJ have been hypothesized to be controlled by barotropic anticyclonic anomalies occurring over the mid-latitudes of the Eurasian continent (Ding & Wang, 2005). Two of these anomalies are located to the west of the TP and over northeast Asia (Krishnan et al., 2009; Wang et al., 2001).

For the late Cenozoic, changes in hydroclimate over continental Asia are usually interpreted as changes in the Asian monsoons (e.g., Chen et al., 2013; He et al., 2021; Li, Ehlers, Werner, et al., 2016; Wang et al., 2019, 2020), the WJ (Fang et al., 2020; Han et al., 2014; Zhang et al., 2018), or both (Ao et al., 2021; Cheng et al., 2012; Chiang et al., 2020). For interglacial/interstadial, for example, mid-Pliocene or mid-Piacenzian, significant shifts in large-scale atmospheric dynamics in both the tropics and mid-latitudes have been detected using climate models and proxy data (Sun et al., 2013), ultimately leading to increases in the global mean precipitation rates as well as the monsoon index (Tan et al., 2020). In contrast, both paleoclimate simulations and proxy data for the glacial/stadial, for example, the Last Glacial Maximum (LGM), show a generally dry climate over the Asian continent with locally increased precipitation (Braconnot et al., 2007; Sun, Wu, Kageyama, et al., 2021). This is explained by low atmospheric moisture content as the main thermodynamic control on the lower LGM regional precipitation rates, with enhancement of horizontal moisture transport responsible for the local precipitation increase (Sun, Wu, Kageyama, et al., 2021). However, the nature, magnitude, and large-scale drivers of seasonal changes in paleoprecipitation across the TP and CA during the glacial/interglacial remain controversial.

In this study, we investigate the changes in the regional and global atmospheric dynamics, such as the seasonal migration of the WJ and monsoonal circulation. We then evaluate their connection to the regional hydroclimate over the TP and CA for selected time periods during the last ~3 Ma. Through this, we provide insights into the influence of large-scale climatic processes on moisture transport to the TP and CA during interglacial/interstadial and glacial/stadial periods. We test a hypothesis that the change in WJ position, and the intensity, strength and duration of the EASM, SASM, and the ISM impact precipitation seasonality and thus surface hydroclimate over TP and CA regions for glacial/interglacial periods. For this purpose, we perform high-resolution (~0.75° per grid cell) GCM ECHAM5 (Roeckner et al., 2003) experiments with mid-Pliocene (~3 Ma), LGM (~21 ka), mid-Holocene (~6 ka), and pre-industrial (PI; year 1850) boundary conditions and analyze variations in the global atmospheric circulation that potentially affected the hydroclimate in selected regions.

2. Methods

2.1. Paleoclimate Simulation Setup

We use the atmospheric GCM ECHAM5 to perform paleoclimate experiments at a high spectral resolution of T159 (corresponding to a horizontal grid spacing of ~0.75° or ~80 km at the equator), 31 vertical levels (up to 10 hPa) and 6 hr output interval. A detailed description of the ECHAM5 model is provided by Roeckner et al. (2003). The pre-industrial (year 1850) control simulations (ECHAM5_PI) was performed using (Dietrich et al., 2013; Etheridge et al., 1996, 1998; Lorenz & Lohmann, 2004; Sowers et al., 2003) sea surface temperatures (SSTs) and sea ice concentrations (SICs) derived from transient coupled ocean-atmosphere simulation (Dietrich et al., 2013; Lorenz & Lohmann, 2004) (Table 1; Figure S1 in Supporting Information S1). Following Dietrich et al. (2013), the greenhouse gas (GHG) concentrations are taken from ice-core-based reconstructions: CO_2 – 280 ppm (Etheridge et al., 1996); CH_4 – 760 ppb (Etheridge et al., 1998); N_2O – 270 ppb (Sowers et al., 2003). Land surface parameters, including vegetation are based on (Hagemann, 2002). When we use the term "climate

Table 1
ECHAM5 Experiments Summary

Experiment name	Reference time	Greenhouse gas concentrations	Orbital parameters	Surface conditions
ECHAM5_PI	Pre-industrial (year 1850)	CO_2 280 ppm, CH_4 760 ppb, N_2O 270 ppb.	eccentricity = 0.016804, obliquity = 23.4725, longitude of perihelion = 278.734	SSTs and SICs from a transient low-resolution coupled ocean-atmosphere simulation of pre-industrial (Dietrich et al., 2013; Lorenz & Lohmann, 2004). Land surface parameters, including vegetation are based on (Hagemann, 2002).
ECHAM5_MH	mid-Holocene (~6 ka)	CO_2 280 ppm, CH_4 650 ppb, N_2O 270 ppb.	eccentricity = 0.018682, obliquity = 24.1048, longitude of perihelion = 180.918	SSTs and SICs from a transient, low-resolution coupled ocean-atmosphere simulation of mid-Holocene (Lohmann et al., 2013; Wei & Lohmann, 2012). Vegetation reconstructions from the BIOME 6000 (Bigelow et al., 2003; Harrison et al., 2001; Pickett et al., 2004; Prentice et al., 2000) serve as a basis for the plant functional types used in the simulation.
ECHAM5_LGM	Last Glacial Maximum (~21 ka)	CO_2 185 ppm, CH_4 350 ppb, N_2O 200 ppb.	eccentricity = 0.018994, obliquity = 22.949, longitude of perihelion = 294.42	SSTs and SICs are based on GLAMAP (Sarnthein et al., 2003) and CLIMAP (CLIMAP Project, 1981) reconstructions for the Atlantic Ocean and Pacific and Indian oceans, respectively. Land– sea distribution and ice sheet extent and thickness were set based on the PMIP III (Abe-Ouchi et al., 2015). Vegetation was reconstructed based on maps of plant functional types from the BIOME 6000 Palaeovegetation Mapping Project (Bigelow et al., 2003; Harrison et al., 2001; Pickett et al., 2004; Prentice et al., 2000) and model predictions by Arnold et al. (2009).
ECHAM5_PLIO	Pliocene (~3 Ma)	CO_2 405 ppm, CH_4 760 ppb, N_2O 270 ppb.	eccentricity = 0.016804, obliquity = 23.4725, longitude of perihelion = 278.734	SSTs, SICs, sea land mask, topography, and ice cover are from PRISM3D (Dowsett et al., 2010; Haywood et al., 2010; Sohl et al., 2009). Vegetation boundary condition was created by converting the PRISM vegetation reconstruction to the JSBACH plant functional types as described by Stepanek and Lohmann (2012).

change" in this manuscript, we refer to climatic departures from our ECHAM5_PI control experiment. Similarly, comparative terms ("higher", "lower", etc.) refer to deviations from ECHAM5_PI values unless explicitly stated otherwise.

We apply ECHAM5 to simulate paleoclimates representing the mid-Pliocene (ECHAM5_PLIO experiment), the LGM (ECHAM5_LGM experiment), and the mid-Holocene (ECHAM5_MH experiment). For all palaeoclimate experiments and the ECHAM5_PI control experiment, we follow the setup of boundary conditions used in Mutz et al. (2018) and the output configuration of Botsyun et al. (2020).

The ECHAM5_PLIO experiment (~3 Ma) provides a possible Asian hydroclimate under higher GHG concentrations, warmer oceans and reduced ice sheets (Table 1). Boundary conditions for the ECHAM5_PLIO simulation, including GHG concentrations (CO_2 405 ppm; CH_4 760 ppb, N_2O 270 ppb), orbital parameters and surface conditions (SSTs, SICs, sea land mask, topography, and ice cover) were taken from the PRISM (Pliocene Research, Interpretation and Synoptic Mapping) project (Dowsett et al., 2010; Haywood et al., 2010;

Sohl et al., 2009), specifically PRISM3D. The ECHAM5_PLIO vegetation boundary condition was created by converting the PRISM vegetation reconstruction to the JSBACH plant functional types as described by Stepanek and Lohmann (2012).

In contrast, the ECHAM5_LGM simulation (~21 ka) allows us to explore the climate response to "cold" boundary conditions comprising large ice sheets, cold oceans, and lower GHG concentrations. ECHAM5_LGM land–sea distribution and ice sheet extent and thickness were set based on the PMIP III (Palaeoclimate Modeling Intercomparison Project, Phase 3, https://pmip3.lsce.ipsl.fr/) guidelines (Abe-Ouchi et al., 2015). Following Schäfer-Neth and Paul (2003), SSTs and SICs for the ECHAM5_LGM are based on GLAMAP (Sarnthein et al., 2003) and CLIMAP (CLIMAP Project, 1981) reconstructions for the Atlantic Ocean and Pacific and Indian oceans, respectively. The differences in SSTs for paleotime slices compared to PI are presented on Figure S1 in Supporting Information S1. LGM vegetation was reconstructed based on maps of plant functional types from the BIOME 6000 Palaeovegetation Mapping Project (Bigelow et al., 2003; Harrison et al., 2001; Pickett et al., 2004; Prentice et al., 2000) and model predictions by Arnold et al. (2009). GHG concentrations for the LGM (CO_2 185 ppm, CH_4 350 ppb, N_2O 200 ppb) were determined according to Otto-Bliesner et al. (2006). Orbital parameters for LGM were set according to Otto-Bliesner et al. (2006).

Sea surface boundary conditions for the ECHAM5_MH (~6 ka) were taken from a transient, low-resolution coupled ocean-atmosphere simulation of the mid-Holocene (Lohmann et al., 2013; Wei & Lohmann, 2012). GHG concentrations (CO_2 – 280 ppm, CH_4 – 650 ppb, N_2O – 270 ppb) were taken from ice core reconstructions of Etheridge et al. (1998, 1996) and Sowers et al. (2003). Orbital parameters were set according to Dietrich et al. (2013). ECHAM5_PLIO, ECHAM5_LGM, and ECHAM5_MH thus represent two end-members and a more intermediate climate, respectively. Each experiment was conducted for 18 model years, including the 3 years required for model spin-up. Our analyses are based on daily and seasonal values of precipitation, evaporation, specific humidity, pressure, and 3D winds. These are constructed through the calculation of arithmetic means of the 6-hourly GCM output.

2.2. Paleoclimate Simulation Analysis

2.2.1. Vertically Integrated Moisture Flux

Vertically integrated moisture flux (VIMF) into and out of a region, together with precipitation, evaporation, and precipitable water, describes important aspects of the hydrological cycle over a region (e.g., Fasullo & Webster, 2003). Following Fasullo and Webster (2003) we calculate zonal (east-west) (Q_λ) and meridional (north-south) (Q_ϕ) components of VIMF for zonal (u) and meridional (v) components of the wind vector V = (u, v). These are calculated as:

$$Q_\lambda = \frac{1}{g}\int_{p2}^{p1} qu\, dp$$
$$Q_\phi = \frac{1}{g}\int_{p2}^{p1} qv\, dp,$$

where q is the specific humidity, g is the gravitational acceleration, p is the atmospheric pressure, $p1$ is the surface pressure, and $p2$ is pressure at 300 hPa. We choose this pressure level because specific humidity above the 300 hPa level is small in all our simulations (not shown) and has no effect on the VIMF (Fasullo & Webster, 2003).

2.2.2. Monsoon Indices

We calculate the East Asian monsoon index (EAMI) as defined by Wang (2002) to describe the intensity of EASM. The EAMI is calculated based on the regional (20°–40°N, 110°–176°E) mean meridional wind velocity anomalies to the climatology at 850 hPa. Analogously, we calculate the South Asian monsoon index (SAMI), which is a unified monsoon index (Li & Zeng, 2002) calculated as the regional (5°–20°N, 70°–110°E) mean meridional wind velocity anomalies to the climatology at 850 hPa. This index has successfully been applied by Li and Zeng (2002) to characterize the seasonal cycle and interannual variability of the monsoon over the South Asian region. We thus consider this index to be suitable for this study.

To determine the intensity and duration of the ISM during the selected time slices, we calculate the horizontal wind shear index (HWSI) as defined by Prasad and Hayashi (2007). The HWSI is calculated by subtracting

the area-averaged 850 hPa zonal wind speeds in a northern region (20°–30°N, 70°–90°E) from area-averaged 850 hPa zonal wind speeds in a more southern region (5°–15°N, 40°–80°E). The HWSI can be used to identify active and inactive ISM days, and thus the onset, withdrawal and duration of the ISM. We follow Mölg et al. (2012), who identified active ISM days when the HWSI value exceeds one standard deviation of the mean. Correspondingly, inactive (break) days are defined as days when the HWSI value is below one standard deviation. We identify the date of the first and last active day as the date of the ISM onset and withdrawal, respectively. The duration is defined as the number of days between the first and last active day. In this study, we calculate all monsoon indices in the same way for all paleoclimate simulations to maintain consistency.

2.2.3. WJ Stream Counts

To assess the changes in position and strength of the high-level (200–300 hPa) WJ over the region in the Late Cenozoic, we construct the occurrence-based jet climatology (jet counts) from ECHAM5 wind fields for each of the performed experiments. We follow the method described in Schiemann et al. (2009). For each time interval (t) a jet event occurs at the current longitude (x) if the value of the zonal wind speed component (u) from the horizontal wind velocity vector V(t, x, y, p) = [u(t, x, y, p), v(t, x, y, p)] satisfies three conditions: (a) the wind vector has a westerly direction ($u > 0$ m s^{-1}), (b) the wind magnitude is a local maximum among all latitudes (y) and pressure levels (p) ($|u|_{t,x}(y,p)$ is a location maximum), and (c) the wind magnitude exceeds 30 m s^{-1} (i.e., $|u| > 30$ m s^{-1}). Identification of the jet axis locations is performed in a spatial domain covering 10°–60°N and 60°–120°E (500–100 hPa). The 15-year climatologies of daily wind speeds from the different paleoclimate simulations provide the basis for this identification. Finally, we follow Schiemann et al. (2009) to conduct a composite analysis for investigating a possible systematic covariation between the position of the WJ in the TP region and the spatial distribution of precipitation in CA. For this analysis, we assign the days to the composite of the northern jet location when the jet (between 80° and 90°E) is north of 38°N, and we assign it to the composite of the southern jet location when the jet is south of 34°N. The averaged precipitation for each of these two sets of days is referenced as "precipitation composite".

2.2.4. Correlation Analysis

To measure the empirical relationship between regional precipitation (over the TP and CA) and monsoon indices (HWSI, EAMI, SAMI), and between regional precipitation (over TP and CA) and latitudinal position (averaged over 75°–80°E) of the WJ, we calculate the Pearson correlation coefficient. These are calculated based on monthly-averaged values of corresponding variables for 15 model years. The significance of correlation is assessed using a t-test.

3. Results

3.1. Changes in Precipitation Amount and Seasonality During Selected Time Periods

The present-day interior of CA, including the Tarim Basin, the Taklimakan Desert and the Gobi desert, are characterized by extremely arid (0.02–0.1 mm day^{-1}) conditions. Our ECHAM5_PI control experiment simulates precipitation rates of ≤1.2 mm day^{-1} over CA (Figure 1a), which is in general agreement with the low observed present-day rainfall. In addition to the small precipitation amount, relatively high evaporation rates (~0.45 mm day^{-1}, not shown here) are also characteristic for this region. The central TP and adjacent regions in the interior of Asia, that is, Northern Tibet and Qinghai, are also characterized by low average rainfall of ≤2.5 mm day^{-1} in our simulation (Figure 1a). However, precipitation rates of ~0.5 mm day^{-1} in DJF and ~3.5 mm day^{-1} in JJA exceed those of CA (compare Figure 1e and Figure 1f).

In our paleoclimate simulations both precipitation amount and its spatial distribution deviate significantly from ECHAM5_PI values in certain seasons (Figure 2). While maximum precipitation occurs during the summer in all simulations, JJA precipitation over the TP is lower in the ECHAM5_LGM simulation (Figure 2h). In contrast, simulated JJA precipitation for ECHAM5_MH and ECHAM5_PLIO experiments is 0.5–1 mm day^{-1} higher than in the ECHAM5_PI experiment (Figures 2g and 2j). High precipitation seasonality is characteristic for both of the selected regions (Figures 1e and 1f) for all time slices. However, the onset, peak and duration vary between our simulations. The "rainy season" (season with precipitation rate >1 mm day^{-1} for the TP and >0.4 mm day^{-1} for CA) in the ECHAM5_LGM simulation is shorter than that of the ECHAM5_PI simulation with maximum ECHAM5_LGM precipitation rates simulated from May until September. Furthermore, precipitation seasonality

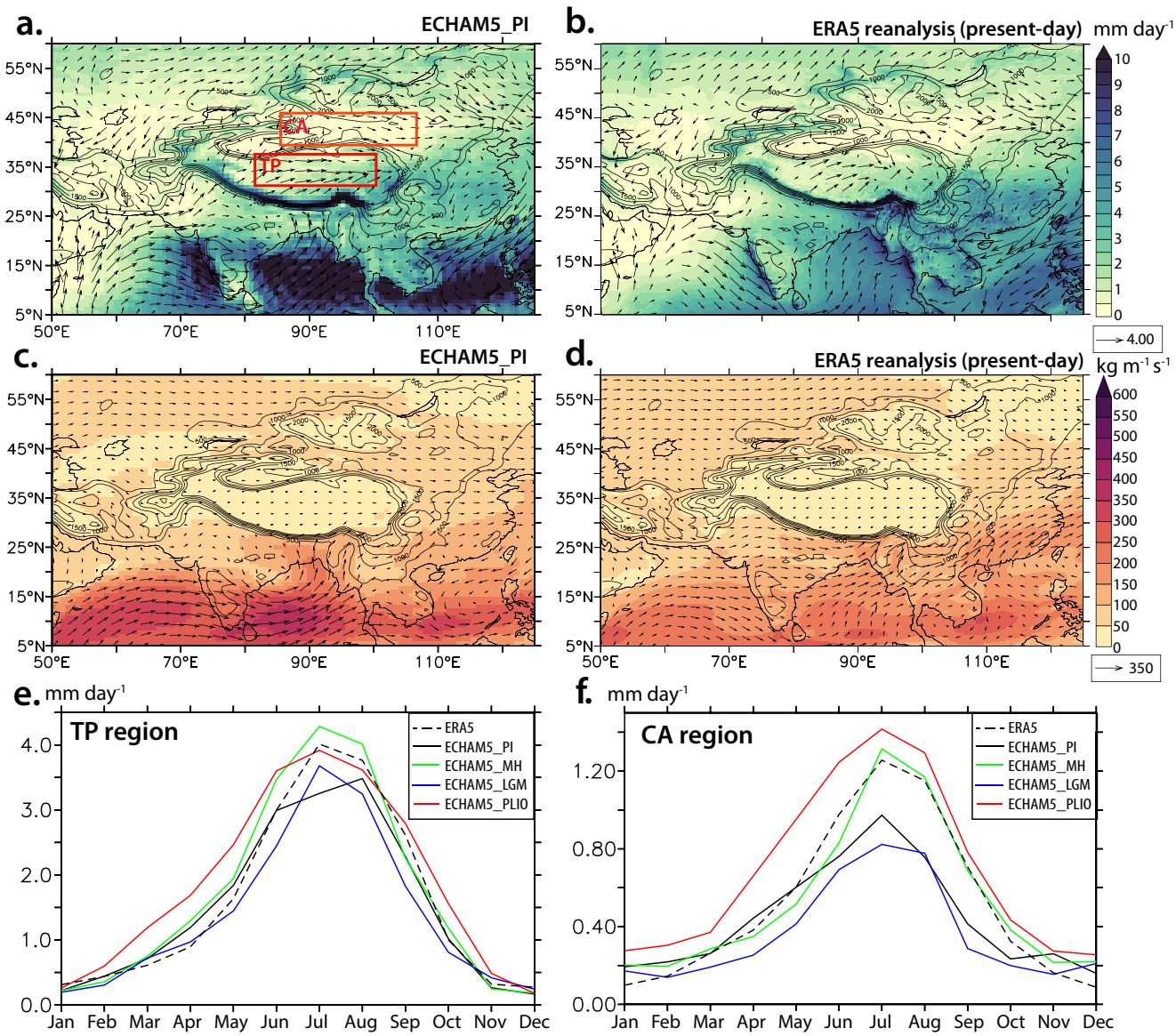

Figure 1. (a) ECHAM5 simulated annual averaged precipitation rates (mm day^{-1}) and wind speed at 2 m level (vectors) (m s^{-1}) for the ECHAM5_PI control simulation, (b) ERA5 reanalysis total precipitation rates and wind speed (vectors) averaged between 1979 and 2019 years; (c), (d) vertically integrated moisture transport (kg m^{-1} s^{-1}), magnitude (shade), and directions (vectors) in (c) ECHAM5_PI, and (d) ERA5 reanalysis (years 1979–2019); (e), (f) seasonal cycle of simulated 15-year averaged precipitation for ECHAM5_PI (black), ECHAM5_LGM (blue), ECHAM5_PLIO (red) experiments, and for ERA5 reanalysis (years 1979–2019, dashed black) for selected regions: (e) TP – central Tibetan Plateau and (f) CA – Central Asia region. Black solid lines on subplots (a–d) show coastlines and topography isolines; isolines are from 500 m, with a 500-m contour interval.

is weakened in the ECHAM5_LGM simulation (Figures 1e and 1f). In contrast, the "rainy season" in the ECHAM5_PLIO simulation is prolonged and starts in March and ends in October. Precipitation seasonality in ECHAM5_PLIO experiment in the chosen domains is enhanced by higher (0.5–0.6 mm day^{-1} for TP and CA) precipitation especially during the months MJJAS (Figures 1e and 1f).

3.2. Vertically Integrated Moisture Flux (VIMF) Changes

The ECHAM5_PI control simulation is able to reproduce the pattern and magnitude of the ERA5 reanalysis-based VIMF (Figures 1c and 1d). We present the change in VIMF over time with particular emphasis on domains that are potential sources of advection of moisture into the TP and CA regions. These include the westerlies (area (i) on Figure 3a), the Indian monsoon (area (ii) on Figure 3a), East Asian monsoon (area (iii) on Figure 3a), and

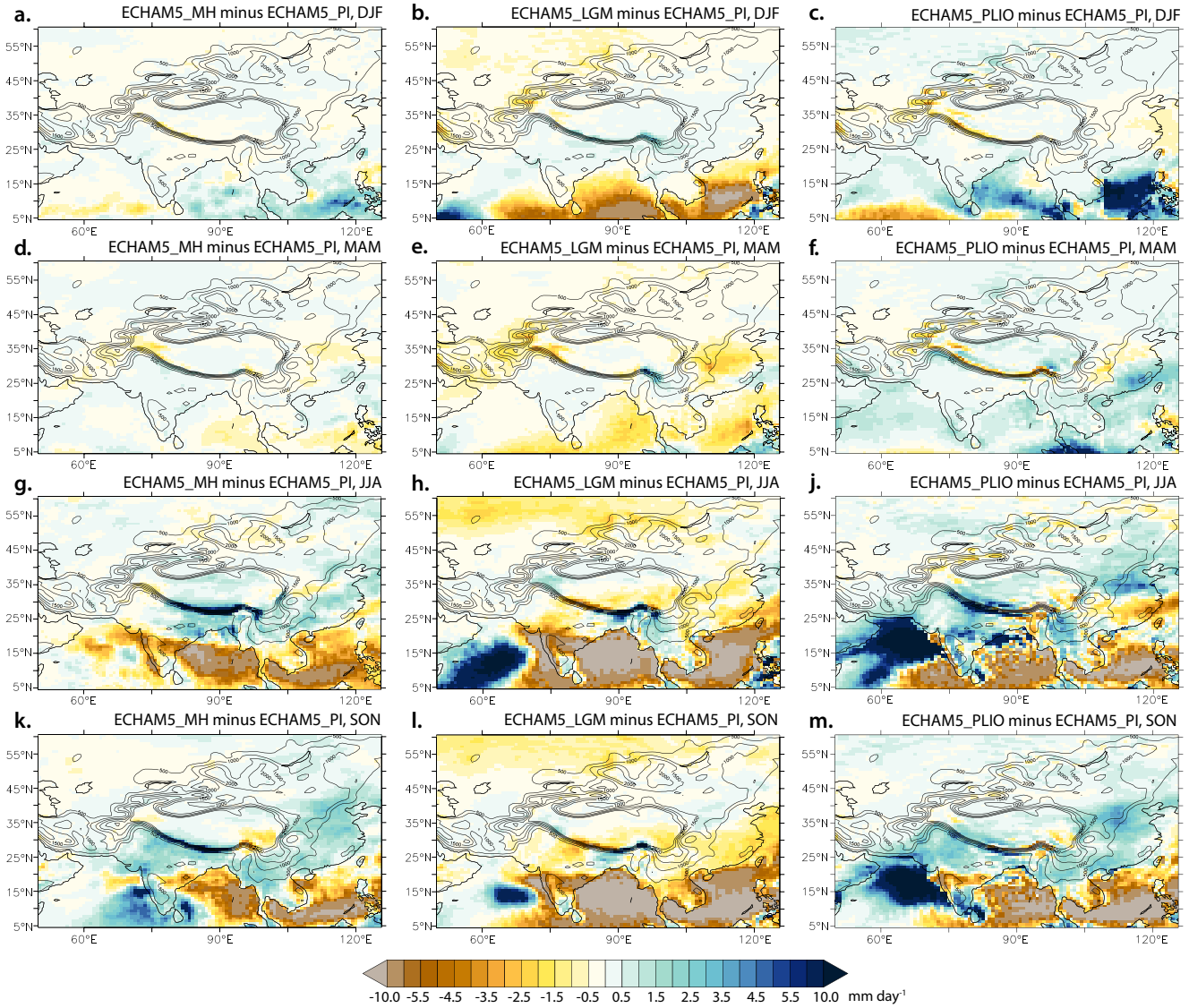

Figure 2. ECHAM5 simulated difference in seasonal mean precipitation rates (mm day^{-1}) between the ECHAM5_PI control experiment and ECHAM5_MH (a, d, g, k), ECHAM5_LGM (b, e, h, l), and ECHAM5_PLIO (c, f, j, m). Black solid lines show coastlines and topography isolines; isolines are from 500 m, with a 500-m contour interval.

South Asian monsoon (area (iv) on Figure 3a) domains. The last includes the Arabian Sea, Bay of Bengal, South India and South-East China. In these four domains, VIMF varies as follows:

1. **Westerlies domain**: In the ECHAM5_LGM simulation, VIMF is > 40 kg m^{-1} s^{-1} lower for all seasons throughout the year (Figures 3b, 3e, 3h, and 3l). In contrast, the maximum VIMF of the ECHAM5_PLIO experiments increase between ~20 kg m^{-1} s^{-1} (DJF and SON, Figures 3c and 3m) and 60 kg m^{-1} s^{-1} (JJA, Figure 3j). In ECHAM5_MH, the VIMF increases to ≤20 kg m^{-1} s^{-1} over the domain in JJA, while other seasons do not show notable changes in the VIMF.
2. **Indian monsoon domain**: All time slice simulations predict the maximum magnitude of change in the VIMF to occur in JJA (Figures 3g, 3h, and 3j). The western part of the domain experiences an increase of ≤200 kg m^{-1} s^{-1} in the ECHAM5_LGM experiment, due to amplified moisture transport from the Arabian Sea. For the remaining year, changes are small (≤40 kg m^{-1} s^{-1} for MAM in the ECHAM5_LGM and ≤20 kg m^{-1} s^{-1} for all other cases).
3. **East Asian monsoon domain**: The VIMF changes for all geologic periods are smaller in DJF (Figures 3a, 3b, and 3c) than in all other seasons. During MAM, the VIMF increases up to 100 kg m^{-1} s^{-1} in the ECHAM5_PLIO

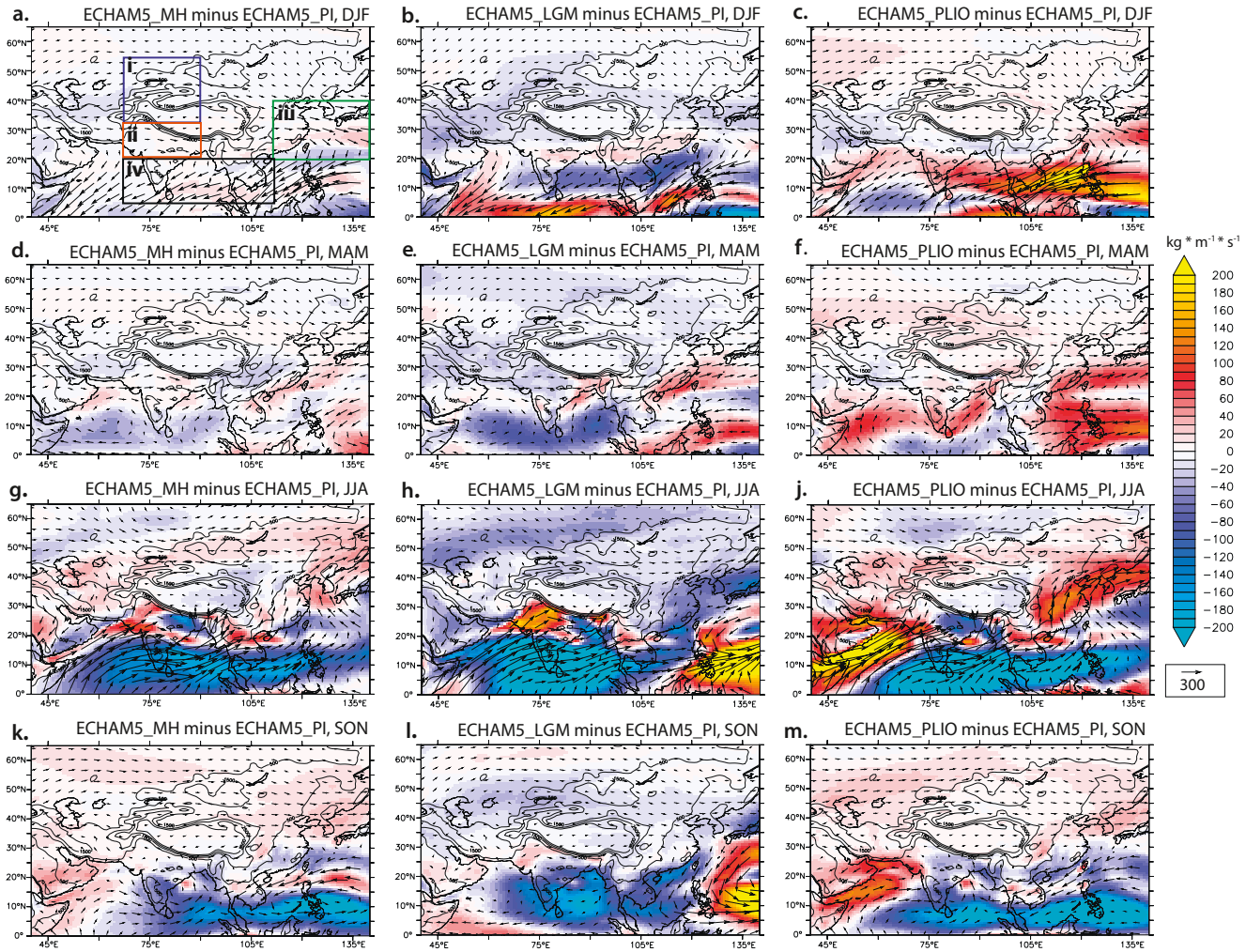

Figure 3. Seasonal (a, b, c – DJF; d, e, f – MAM; g, h, j – JJA; k, l, m – SON) mean differences of vertically integrated moisture transport for ECHAM5_MH (a, d, g, k), ECHAM5_LGM (b, e, h, l) and ECHAM5_PLIO (c, f, j, m) experiments compared to ECHAM5_PI. The vectors show corresponding seasonal mean directions of the intensity of vertically integrated moisture transport for ECHAM5_MH (a, d, g, k), ECHAM5_LGM (b, e, h, l) and ECHAM5_PLIO (c, f, j, m) experiments. The rectangles on subplot (a) correspond to the (i) westerlies, (ii) Indian monsoon, (iii) East Asian monsoon, and (iv) South Asian monsoon domains. Black solid lines show coastlines and topography isolines; isolines are from 500 m, with a 500-m contour interval.

(Figure 3f). In JJA, the VIMF over the continental part of southeast China is higher in ECHAM5_PLIO and lower in ECHAM5_LGM with the magnitudes of the difference exceeding 100 kg m^{-1} s^{-1} (Figures 3e and 3f). The SON VIMF pattern of changes over the East Asian monsoon domain is similar to that of JJA, but the magnitude of change is smaller (Figures 3k, 3l, and 3m). The ECHAM5_LGM is an exception to this and documents increase in northeast-southwest flux over the East China Sea.

4. **South Asian monsoon domain:** All time slice experiments predict a reduction (>300 kg m^{-1} s^{-1}) of westerly moisture transport during JJA and SON (Figures 3g–3m). The MAM VIMF decreases over the eastern Bay of Bengal by 20–40 kg m^{-1} s^{-1} for the ECHAM5_MH and ECHAM5_PLIO and by ≤ 100 kg m^{-1} s^{-1} for the ECHAM5_LGM. The ECHAM5_LGM simulation of DJF VIMF predicts a ∼100 kg m^{-1} s^{-1} decrease in easterly water transport, whereas the ECHAM5_PLIO simulation predicts an increase in easterly water transport of >150 kg m^{-1} s^{-1} over the domain (Figures 3b and 3c).

3.3. EASM, SASM, and ISM Changes

Monsoon indexes for the East Asian, South Asian, and ISM are lowest in the ECHAM5_LGM simulation, where EAMI, SAMI, and HWSI values are reduced by 33%, 39%, and 72%, respectively (Figure 4). Low-level (850 hPa)

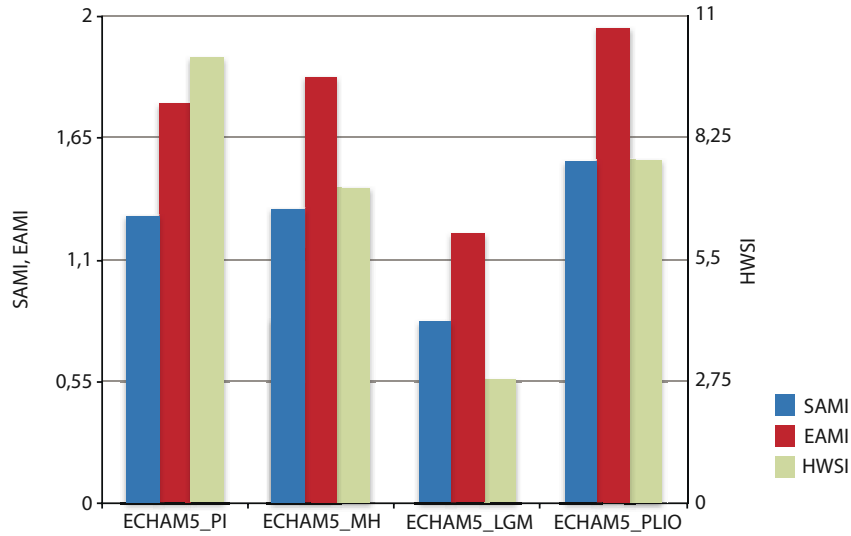

Figure 4. Monsoon strength index values based on the simulated long-term annual means the ECHAM5_PI, ECHAM5_MH, ECHAM5_LGM, and ECHAM5_PLIO experiments. The East Asian monsoon index (EAMI), South Asian monsoon index (SAMI) and horizontal wind shear index (HWSI) are calculated following Wang (2002), Li and Zeng (2002), and Prasad and Hayashi (2007), respectively.

wind speeds also decrease in the ECHAM5_LGM simulation. In contrast, ECHAM5_PLIO values for SAMI and EAMI increase by 18%, while ECHAM5_PLIO HWSI values decrease by 23% (Figure 4). Changes in the ECHAM5_MH monsoon SAMI and EAMI index values are minimal (6% and 2%), while ECHAM5_MH HWSI decreases by 30%.

The maximum, uninterrupted duration of the ISM, as derived from HWSI, is 114 (±8) days for the ECHAM5_PI control experiment, while the minimum duration is 44 (±8) days in the ECHAM5_LGM. The onset of the ECHAM5_LGM monsoon is in early June, while the withdrawal is as early as in August. For the ECHAM5_MH and ECHAM5_PLIO experiments, the duration was estimated to be 100 (±6) and 107 (±11) days, respectively. In both simulations, the ISM starts in early June and ends in late September.

3.4. Mid-Latitude WJ Stream

The ECHAM5_PI simulation shows a shift of the core of the highest wind speed from its southern position in the spring (April to May) to a northern position in summer (June to September) and back to a southern position in autumn (October) (Figure 5). This shift also occurs in the ECHAM5_MH, ECHAM5_LGM, and ECHAM5_PLIO experiments. However, in the ECHAM5_PLIO simulation, the WJ shifts to a northerly position earlier in the year (April) and remains in a northerly position until October (Figure 5). In contrast, in the ECHAM5_LGM, the WJ axis shifts to the north later in the year and returns at a similar time, thus shortening the duration of northerly position of the WJ. Moreover, the ECHAM5_LGM experiment shows a reduction of the mean zonal flow by 2–10 m s^{-1} in the TP, CA and the Westerlies domain for all seasons.

Comparisons of computed seasonal occurrence-based jet climatologies (jet counts) highlight several differences between our paleoclimate simulations. In DJF, the ECHAM5_MH simulation yields a higher (>20 days) jet count south of TP over the Nepal region and a lower jet count over Southwest China (Figure 6a). In the ECHAM5_LGM experiment, the core of the jet has a more southerly position over Asia in DJF, resulting in a "bipolar" anomaly (Figure 6b). In the ECHAM5_PLIO experiment, the difference in jet counts produces a reversed ECHAM5_LGM pattern. The most notable result for MAM is an increase in jet occurrences of ≤10–15 days over the TP region in the ECHAM5_PLIO simulation (Figure 6f). During the JJA (Figures 6g, 6h, and 6j), the ECHAM5_LGM experiment produces a decrease in jet occurrences (≤15 days) north of the TP, while the ECHAM5_MH and ECHAM5_PLIO simulations predict an increase over the Tian Shan region.

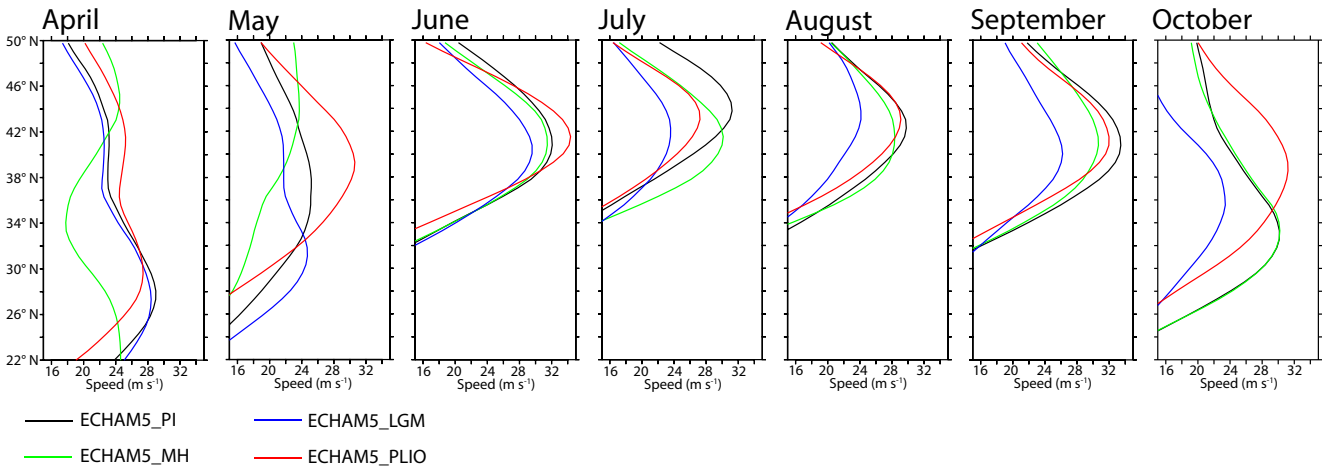

Figure 5. Monthly meridional profiles (averaged over 75°–80°E) of zonal wind speed at 200 hPa monthly from April to September show the latitudinal shift of the WJ in the ECHAM5_PI (black), ECHAM5_MH (green), ECHAM5_LGM (blue), and ECHAM5_PLIO (red) simulations.

The composite analysis (following Schiemann et al., 2009) (Figure 7) shows a systematic covariation between the position of the WJ in the TP region and the spatial distribution of precipitation in CA for all selected time slices. In April, a northerly (southerly) jet position over the TP is associated with higher (lower) precipitation rates to the north of the Plateau, and lower (higher) precipitation rates over the Plateau itself for ECHAM_PI, ECHAM5_MH, and ECHAM5_PLIO. For the ECHAM5_LGM simulation, a northerly position of the WJ is associated with higher precipitation rates to the north of Plateau and lower precipitation rates over the northern flanks of the Plateau. Following Schiemann et al. (2009), we consider these composites over the TP and CA robust and independent from the influence of the seasonal cycle.

3.5. Correlation Between Regional Precipitation, HWSI, EAMI, SAMI, and the Latitudinal Position of the WJ Stream

Over both the TP and CA, precipitation is positively correlated with HWSI, EAMI and SAMI on an annual time scale for all paleoclimate time slices (Table 2). Over the TP, the highest Pearson correlation coefficient (r) between HWSI and regional precipitation is calculated for ECHAM5_PI and ECHAM5_LGM ($r = 0.85$). For ECHAM5_MH and ECHAM5_PLIO experiments, the correlation yields lower coefficients of $r = 0.81$ and $r = 0.80$, respectively. The Pearson correlation between EAMI and regional precipitation over TP is weakest for ECHAM5_LGM ($r = 0.45$), while for ECHAM5_PI, ECHAM5_MH, and ECHAM5_PLIO, the coefficients are $r = 0.81$, $r = 0.87$, and $r = 0.85$, respectively. The Pearson correlation coefficients between SAMI and regional precipitation are $r = 0.80$, $r = 0.79$, $r = 0.62$, and $r = 0.86$ for ECHAM5_PI, ECHAM5_MH, ECHAM5_LGM, and ECHAM5_PLIO, respectively.

Over CA, the correlation between HWSI and regional precipitation is highest for ECHAM5_LGM ($r = 0.80$), and lower for ECHAM5_PI, ECHAM5_MH ($r = 0.67$) and ECHAM5_PLIO ($r = 0.61$). The correlation between EAMI and regional precipitation over CA is weakest for ECHAM5_LGM ($r = 0.42$), while for ECHAM5_PI, ECHAM5_MH, and ECHAM5_PLIO, the coefficients are $r = 0.71$, $r = 0.72$, and $r = 0.75$, respectively. The Pearson correlation coefficients between SAMI and regional precipitation are $r = 0.69$, $r = 0.60$, $r = 0.57$, and $r = 0.69$ for ECHAM5_PI, ECHAM5_MH, ECHAM5_LGM, and ECHAM5_PLIO, respectively.

Precipitation over the TP and CA is also positively correlated with the WJ latitudinal position for all paleoclimate time slices. Over the TP, the Pearson correlation coefficients between precipitation and WJ latitudinal position are $r = 0.68$, $r = 0.63$, $r = 0.70$, and $r = 0.64$ for ECHAM5_PI, ECHAM5_MH, ECHAM5_LGM, and ECHAM5_PLIO, respectively. For CA, the corresponding correlation is weaker, yielding coefficients of $r = 0.48$ (ECHAM5_MH), $r = 0.58$ (ECHAM5_LGM), $r = 0.54$ (ECHAM5_PI), and $r = 0.56$ (ECHAM5_PLIO).

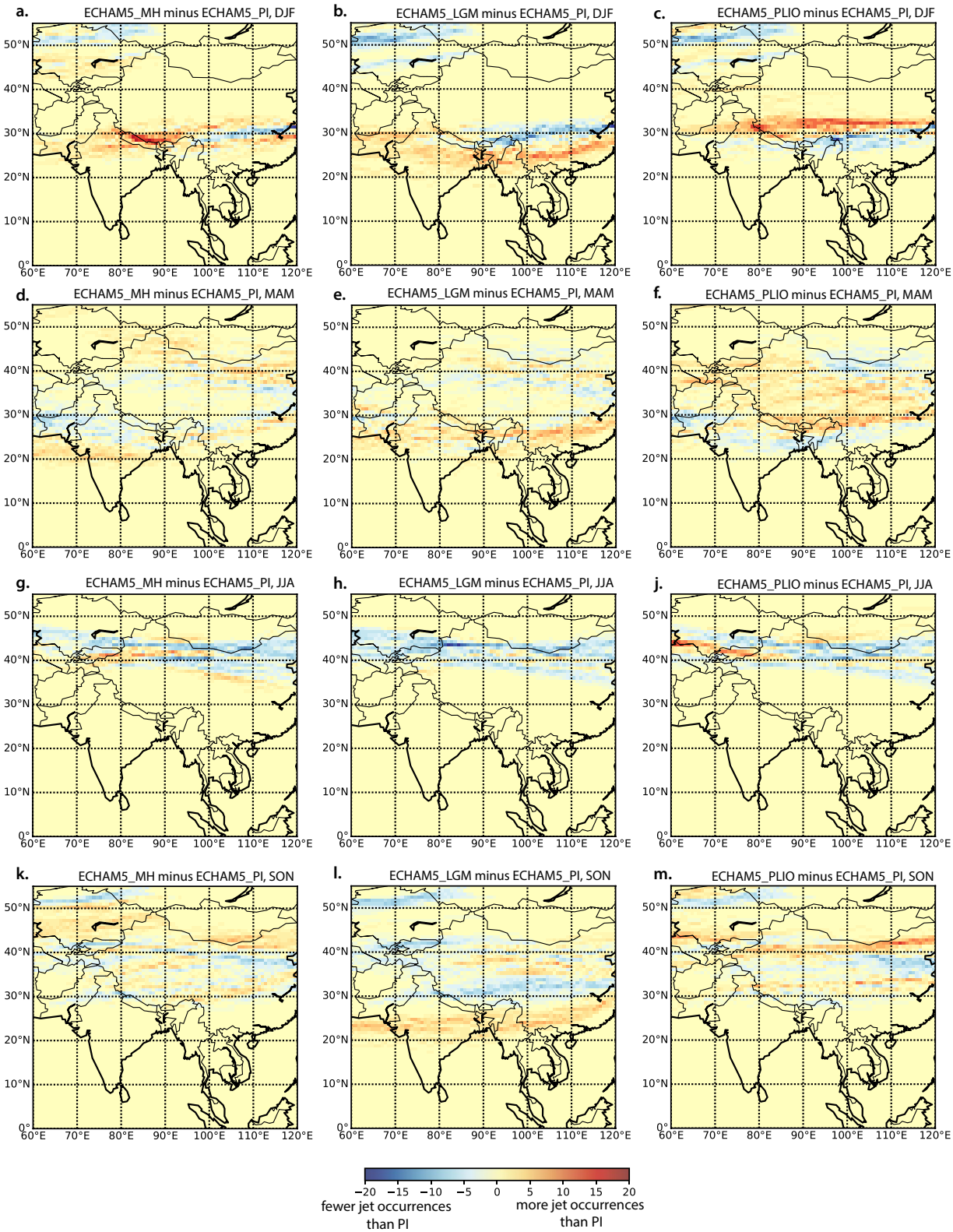

Figure 6. Seasonally (a, b, c – DJF; d, e, f – MAM; g, h, j – JJA; k, l, m – SON) averaged differences in jet counts (days), following the method of Schiemann et al. (2009). Jet counts are calculated for the ECHAM5_MH (a, d, g, k), ECHAM5_LGM (b, e, h, l), and ECHAM5_PLIO (c, f, j, m) experiments. Differences are shown relative to ECHAM5_PI.

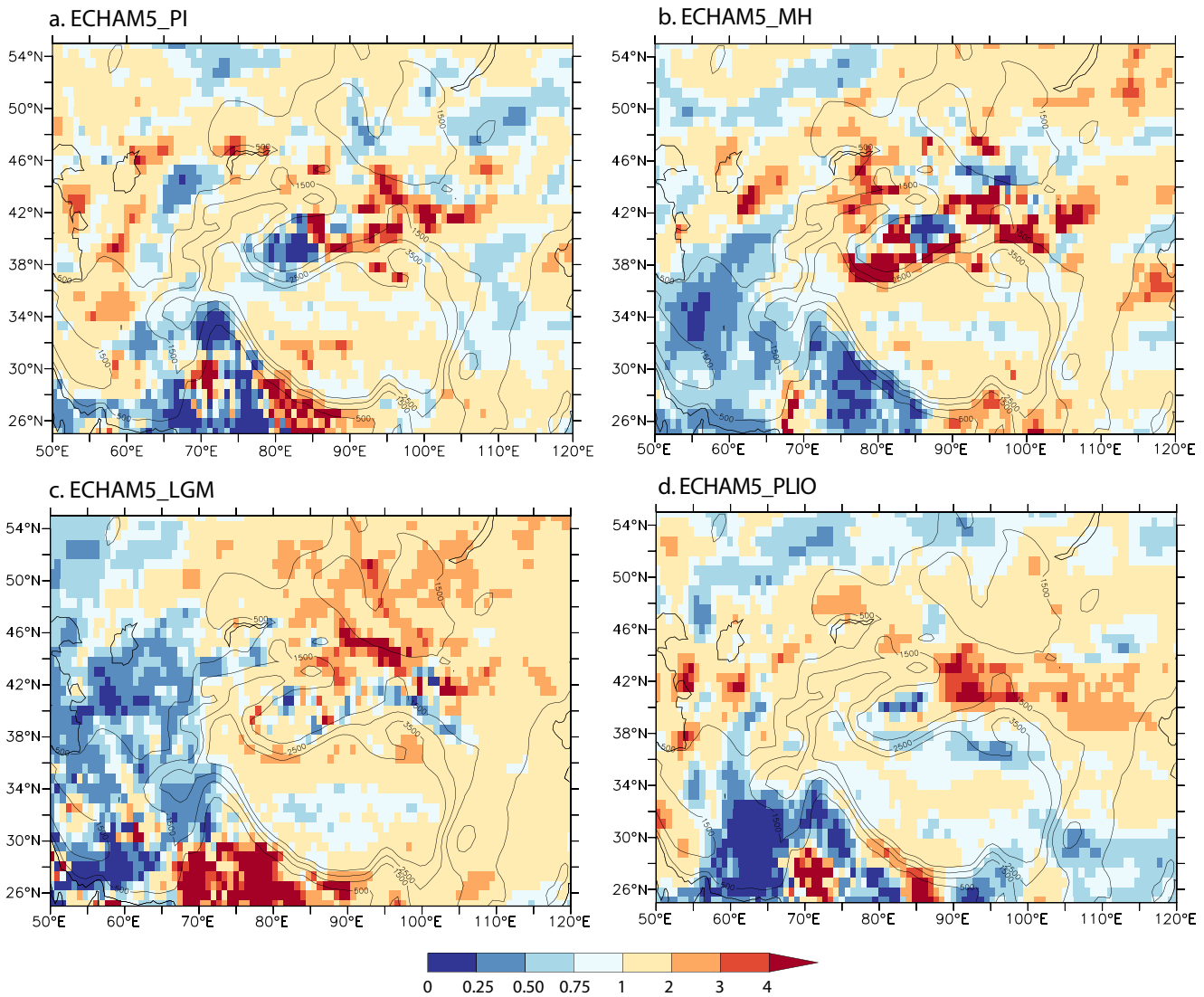

Figure 7. Ratio between precipitation composites for days in April, when the WJ is located north of the Tibetan Plateau (between 80° and 90°E) and for days when the WJ is located south of the Tibetan Plateau (between 80° and 90°E) for (a) ECHAM5_PI, (b) ECHAM5_MH, (c) ECHAM5_LGM, and (d) ECHAM5_PLIO experiments. Black solid lines topography isolines from 500 m, with a 500-m contour interval.

4. Discussion

4.1. Shift of the WJ Stream and Its Link to Regional Hydroclimate

The relationship between the WJ position and Asian surface climate has been suggested by previous studies based on both observations and models (Bothe et al., 2012; Du et al., 2016; Gong & Ho, 2003; Hurrell, 1995, 1996; Mölg et al., 2017; Sampe & Xie, 2010; Schiemann et al., 2009; Zhao et al., 2014). Our modeling results support existing studies (Löfverström et al., 2016; Toggweiler & Russell, 2008; Williams & Bryan, 2006) showing a ~10° latitudinal shift of the Northern Hemisphere high-level WJ axis toward the equator during glacial and stadial periods (Figure 5). The simulated shift over the entrance region in MAM, JJA, and SON is consistent with the moisture input to the region. For example, the LGM experienced fewer jets (Figures 6e, 6h, and 6l) and reduced moisture transport over the latitudes north of 35°N during the corresponding seasons (Figures 3e, 3h, and 3l). A likely cause of this shift is a decreased thermal contrast in the atmosphere in response to lower CO_2 levels (Toggweiler & Russell, 2008; Williams & Bryan, 2006).

Table 2
Mean Pearson Correlation Coefficients r; Confidence Level of 95%) Between Monthly-Averaged Precipitation Over TP and CA Regions and Monthly-Averaged HWSI, EAMI, SAMI, and Averaged Latitudinal Position of WJ for Corresponding Simulations

	HWSI				EAMI				SAMI				WJ latitude			
	ECH AM5 _PI	ECH AM5 _MH	ECH AM5 _LGM	ECH AM5 _PLIO	ECH AM5 _PI	ECH AM5 _MH	ECH AM5 _LGM	ECH AM5 _PLIO	ECH AM5 _PI	ECH AM5 _MH	ECH AM5 _LGM	ECH AM5 _PLIO	ECH AM5 _PI	ECH AM5 _MH	ECH AM5 _LGM	ECH AM5 _PLIO
CA	0.57	0.67	0.80	0.61	0.71	0.72	0.42	0.75	0.69	0.60	0.57	0.69	0.54	0.48	0.58	0.56
TP	0.85	0.81	0.85	0.80	0.81	0.87	0.45	0.85	0.80	0.79	0.62	0.86	0.68	0.63	0.70	0.64

The position of the WJ is closely tied to climatological seasonal cycles in moisture transport (Herzschuh et al., 2019; Kapp et al., 2011). More specifically, when the WJ is tilted toward the pole during the rainy season, northward moisture transport is strengthened in the East Asian monsoon region (Sampe & Xie, 2010). For the mid-Pliocene we simulate an enhanced westward moisture flux from the Philippine Sea in MAM, JJA, and SON that coincides with the prolonged northward position of the WJ. Moreover, for the mid-Pliocene during MAM and SON, more jets occur over the northern TP in comparison to pre-industrial times, which is also consistent with the increase in moisture transport. In contrast, the simulated reduction in moisture transport over continental China in the LGM for MAM and SON is consistent with the delayed WJ transition through the year. In addition, the simulated shift in the latitudinal position of the WJ over the entrance region to CA and the High Asia region (from 40° to 50°N and from 70° to 80°E) during MAM, JJA, and SON time is consistent with the moisture input to the region. During the LGM, our simulation yields fewer jets over the entrance region, which fits the reduced moisture transport over the latitudes north of 35°N during the corresponding seasons.

For the present-day, Bothe et al. (2011, 2012) suggested a strong link between the seasonal position of the upper troposphere WJ and the amount of precipitation over the TP and CA. They also note a regional precipitation peak that coincides with the northern position of the WJ. In our simulations higher precipitation rates temporally coincide with the northern position of the WJ (Figures 1 and 5). More specifically, we show that during warm periods (e.g., mid-Pliocene or interglacial), the WJ migrates northward earlier in the year (in late April) and reaches higher latitudes than in the pre-industrial. This coincides with increased local precipitation over the TP and CA. During cooler periods (the LGM), the WJ migrates northward later in the year (June) and remains over lower latitudes than during warmer periods, resulting in a drier CA. For all simulations, local precipitation over the TP and the CA shows a significant positive correlation with the latitudinal position of the WJ axis (Table 2). Our results suggest that the findings by Bothe et al. (2011, 2012), as well as the underlying mechanisms, extend to Late Cenozoic climates.

All experiments predict the highest precipitation rates between May and September. These are highest for the mid-Pliocene and lowest for the LGM over the TP and CA. These findings are consistent with paleohydrological data, which indicate drier conditions during glacial and wetter conditions during interglacial periods (An et al., 2012; Chen et al., 2008; Zhao et al., 2017). In addition, our models predict a longer rainy season in the mid-Pliocene (from April till October) and shorter rainy season in the LGM (from June to August). This seasonality change corresponds to an altering timing of the northward evolution of the WJ due to the already discussed link between precipitation and WJ.

4.2. Monsoons Changes and Their Link to Regional Hydroclimate

Present-day northern TP and CA are often considered to receive moisture predominantly via the mid-latitude westerlies, while southerly (likely monsoonal) moisture rarely reaches regions north of the central Tibet (Caves Rugenstein & Chamberlain, 2018). However, some studies suggest a dynamic link between the Indo-Asian monsoon circulation and local hydroclimate (Ding & Wang, 2005; Saeed et al., 2011). Moreover, past changes in regional hydroclimate over the northeastern TP are often interpreted as shifts in the Indo-Asian monsoons (e.g., Cheng et al., 2012). Wang, Schmidt, et al. (2021) concluded that the difference in the moisture budget in the Qaidam Basin between the mid-Pliocene and the present is due to a combined effect of changes in the mid-latitude westerlies and the EASM. In general, regions influenced by the EASM have been shown to experience increased precipitation rates in the Pliocene, even in regions dominated by the mid-latitude storm tracks (Haywood et al., 2013). We find a positive correlation between ISM, EASM, and SASM and local precipitation over both the TP and CA for all paleotime slices. Higher precipitation rates in the mid-Pliocene compared to PI coincide with increased moisture transport over the East Asian monsoon domain. In contrast, decreased moisture transport over the Bay of Bengal and Southeast China is associated with lower precipitation rates over the TP and CA for all seasons. The extended (shortened) "rainy season" for the mid-Pliocene (LGM) over TP and CA is also consistent with the extended (shortened) duration of ISM. Further analysis is required to complement our statistical correlations to identify actual driving forces linking the regional hydroclimate and monsoonal circulation.

4.3. Consequences for Proxy Interpretation

Variations in hydrology-sensitive terrestrial records from the Asian region are classically interpreted as the result of an interplay between the monsoon and westerlies (e.g., An et al., 2012; Chen et al., 2008). Proxy records available from the TP and CA region include sedimentological, biological, isotopic, elemental, magnetic and geomorphologic data (Dettman et al., 2001; Han et al., 2020; Miao et al., 2016; Stauch, 2015; Tang et al., 2000; Zhang et al., 2012). These proxy data are sensitive to changes in hydroclimate and provide a long-term perspective on environmental change in the region. Moreover, proxy records are sensitive to the seasonality of precipitation (e.g., Ronay et al., 2019). Given this, the implications of our results on proxy-records are several-fold. Here, we highlight a few examples and argue that the simulated changes in the seasonal cycle of precipitation across the TP and CA during the selected time slices have potential implications for the interpretation of: ice cores, in situ carbonate $\delta^{18}O$, pollen records, and geomorphological evidence for paleolake levels and other paleoclimate proxy data. Here we discuss the implications of our results for the previously mentioned proxy data types. More specifically:

1. **Ice cores and glacier regimes:** Proxy records from ice cores may be biased toward a particular season due to a change in precipitation distribution (Gildor & Ghil, 2002). Over the TP, glacial regimes are sensitive to the seasonality of precipitation (Fujita, 2008; Mölg et al., 2012). Maussion et al. (2014) proposed a classification of glaciers on the TP based on their accumulation and mass balance. Using a spatial analysis of precipitation seasonality, they concluded that glaciers in different precipitation regimes respond differently to changes in climate and shifts in precipitation seasonality. Our results also stress the consideration of temporal changes in precipitation seasonality over the Late Cenozoic when glacier energy and mass balance changes are investigated through time. For example, a reduced wet season over the northern TP during the LGM would lead to a shift of the seasonal cluster centers proposed by Maussion et al. (2014) toward JJA, a reduced monsoon-related precipitation period in the central and eastern part of the southern TP, and a longer winter precipitation period in the Karakoram.
2. ***In situ* (soil) carbonate $\delta^{18}O$:** $\delta^{18}O$-based paleoclimate reconstructions may be biased toward the wetter season (Ronay et al., 2019). For the TP and CA region, a change in precipitation seasonality likely affects $\delta^{18}O$ measured in carbonates due to shifts in (a) moisture sources, which may have a different $\delta^{18}O$ ratio; (b) pathways between the moisture source and the paleorecord site; (c) condensation and evaporation processes within the atmosphere; and (d) types of precipitation. We demonstrate a shift in the WJ and in precipitation seasonality in the mid-Pliocene that potentially leads to an increase in $\delta^{18}O$ values in April and May. Similarly, if the LGM WJ remained south of Tibet or moved northward later in summer, it will result in a difference in mean annual $\delta^{18}O$ values between LGM conditions and the present-day.
3. **Pollen records:** The distribution of airborne pollen is generally influenced by prevailing wind directions, and thus pollen assemblages vary considerably with the season of deposition (Giner et al., 1999; Zhu et al., 2015). Airborne pollen over specific sites on the TP are controlled by wind direction and air mass trajectories (Zhu et al., 2015). If the mid-Pliocene westerly winds prevail over the TP and CA as early as in April, the WJ may transport more exotic pollen to the TP, such as pollen from the Iranian Plateau.
4. **Water balance and geomorphic evidence for lake levels:** The Late Cenozoic geomorphic evolution of paleolake coastlines may reflect not only the bulk annual precipitation, but also the seasonality of precipitation, which plays a role in the development of extreme lake levels (Lei et al., 2017). Seasonal changes in precipitation, runoff, and evaporation over the lake lead to the formation and persistence of extreme lake levels (Argyilan & Forman, 2003). Our estimates for past shifts in precipitation seasonality should therefore be considered in the interpretation and reconstruction of past lake levels. Another issue is the regional water balance that includes evaporation, precipitation, surface runoff, groundwater storage, and atmospheric humidity influx and loss. Scherer (2020) studied the local climatic driver of net water balance of the Qaidam Basin region in the CA, the mechanism of drying of the Qaidam mega-lake and its possible restoration under warmer and wetter climate. Wang, Schmidt, et al. (2021) further investigated the large-scale controls of water balance in the Qaidam Basin and revealed the role of mid-latitude westerlies and EASM in maintaining the Qaidam mega-lake under the mid-Pliocene climate. Our results are consistent with those of both Scherer (2020) and Wang, Schmidt, et al. (2021), who predict higher mean annual precipitation (or long-term mean) in a mid-Pliocene—like climate across the TP and CA, as well as the possible formation and maintenance of mega-lake systems. However, we further argue that the change in precipitation seasonality should be considered for conclusions regarding the suitability of lakes in arid and hyperarid environments, since for this

case a positive water balance must be maintained throughout the year, rather than a short season of extreme precipitation rates.

4.4. Driving Mechanisms for Glacial-Interglacial Precipitation and Precipitation Seasonality Change in the TP and CA

Based on an analysis of the HAR dataset, Scherer (2020) suggested that the present-day variations in hydroclimate (in both precipitation and precipitation minus evatranspiration) in the Qaidam Basin are mainly caused by changes in specific humidity. According to this work, air temperature is correlated with specific humidity, but is not the driver of precipitation. Therefore, Scherer (2020) concluded that mid-Pliocene climates in the Qaidam Basin would have been more humid and thus come with more precipitation. This finding has later been also demonstrated by Wang, Schmidt, et al. (2021) using dynamical downscaling techniques. They found that specific humidity, precipitation, and net precipitation were higher during the mid-Pliocene, although air temperature was lower in the mid-Pliocene over this region. The results of our GCM experiments confirm that the humidity increase in the mid-Pliocene contributes to higher precipitation rates in the TP and CA. Furthermore, we show that the LGM period was less humid and therefore precipitation was lower. This is further evidence that the relationship between specific humidity and precipitation is robust, at least during the last 3 Ma.

The Northern Hemisphere pressure system changes under increased/decreased GHG concentrations, warmer/cooler oceans, and increased/decreased ice sheet volumes have implications for atmospheric circulation in both the tropics and mid-latitudes (Coumou et al., 2015; Li et al., 2012). The strengthening/weakening of both the ISM and the WJ may be related to changes in the pressure gradients over the North Atlantic (Dugam et al., 1997) and the Eurasian continent (Rajeevan, 2002). Chang et al. (2001); Wu, Li, et al. (2012); Yang et al. (2004) and others suggested a strong influence of the North Atlantic Oscillation (NAO) on the Asian monsoon. Moreover, a teleconnection between the NAO and the surface climate in Asia was found for the present-day climate (Li et al., 2008). In addition, a link between the NAO and the Asian surface climate has been proposed for the LGM (Pausata et al., 2009). However, additional modeling efforts are needed to understand the link between the NAO and surface climate in Asia during the Late Cenozoic. Han et al. (2020) suggested that co-occurrence of low obliquity amplitudes and low eccentricity promoted ice sheet expansion in the Northern Hemisphere and in turn changed the seasonality shift of the WJ. Mölg et al. (2017) argue that investigations of climatic anomalies over Asia should consider the stationary wave structure of the jet. It has been hypothesized that the latitudinal position and occurrence of the WJ are controlled by the barotrophic anticyclonic anomalies over the mid-latitudes of the Eurasian continent (Ding & Wang, 2005). These include one located west of the TP and one over northeast Asia (Krishnan et al., 2009; Wang et al., 2001). This pattern is consistent with the pressure variability anomalies of the Eurasian Wave Train (EWT) (Ding & Wang, 2005; Saeed et al., 2011). For present-day climate, Ding and Wang (2005) suggested a strong connection between ISM precipitation and mid-latitude circulation via the EWT. However, on geological time scales, the EWT and the robustness of the coupling between the EWT, monsoonal circulations and regional precipitation have not been studied. Nevertheless, these are likely important factors to consider in the explanation of shifts in the WJ, precipitation rates and seasonality in the CA and TP region. However, an in-depth study of changes in Northern Hemisphere teleconnection is beyond the scope of this study.

4.5. Uncertainty and Methodological Limitations

This study includes several caveats. We assume that ECHAM5 is able to reproduce aspects of the regional hydroclimate over the TP and CA and the main dynamical features in the atmosphere. While ECHAM5 is able to reproduce modern and paleoclimate, including monsoonal Asian climate (e.g., Knorr et al., 2011; Li, Ehlers, Mutz, et al., 2016; Wang, Schmidt, et al., 2021), mesoscale and fine scale processes that are relevant for regional hydroclimate over land, such as local convection and soil evapotranspiration, are poorly resolved in ECHAM5 (e.g., Cheng et al., 2012).

The ability of ECHAM5 to predict orographic precipitation remains limited, but improves significantly at high model resolution (Meehl et al., 2007). In regions with complex mountain topography, GCMs' predictions of orographic precipitation may be dry biased due to the GCM smoothing of regional topography (Tselioudis et al., 2012). Dynamic downscaling techniques in conjunction with paleoclimate GCM simulations could help improve precipitation prediction (e.g., Wang, Schmidt, et al., 2021). Furthermore, ECHAM5 tends to

underestimate the moisture from the local recycling (Haese et al., 2013). Non-hydrostatic regional models should be used to overcome the uncertainty in the local hydroclimate representation (Kendon et al., 2017). Over the tropical Indian Ocean and the Bay of Bengal, ECHAM5 tends to overestimate precipitation, likely due to incorrect simulation of the low-level moisture and convective processes (Abhik et al., 2014). This may cause precipitation anomalies to persist over the Bay of Bengal for all paleotime slices and seasons. However, the relationship between these anomalies and the local hydroclimate over the TP and CA is unclear.

In our study, we do not aim to quantify the effects of individual boundary conditions on regional hydroclimate (e.g., Kamae et al., 2016; Zhang et al., 2019), but rather to quantify the overall effect and compare it between different paleotime slices. A detailed study of the sensitivity of the hydroclimate of TP and CA to individual boundary conditions also offers an interesting perspective. Furthermore, because the effects of individual boundary conditions were not examined, some important effects could be misinterpreted. For example, we did not explicitly quantify the effects of topographic changes on local hydroclimate, even though the topography of the TP for mid-Pliocene, LGM, and preindustrial shows differences in experimental design. We acknowledge that, for example, the changing topography of the Northern TP and the Tian Shan in the mid-Pliocene compared to preindustrial, affected both the WJ and monsoon and further local hydroclimate (Baldwin & Vecchi, 2016; Zhang et al., 2017). The contribution of the effects of topography on the hydroclimate of the TP and CA relative to global climate drivers should be investigated in more detail in future studies.

Finally, we assume that our metrics to quantify the WJ and monsoon intensity are adequate throughout the Late Cenozoic. An additional source of uncertainties is associated with the choice of boundary conditions for paleosimulations. For example, the model sensitivity to the choice of the orbital and greenhouse forcing for the mid-Pliocene case have been shown in Haywood et al. (2016). For further discussion of potential modeling-related uncertainties, the reader is referred to Mutz et al. (2018) and Botsyun and Ehlers (2021).

In this study we use one model (ECHAM5), but for each study period there is a corresponding Paleoclimate Modelling Intercomparison Project (PMIP). However, it is not our goal to compare our results with the PMIP model experiments. Such a study would of course be of great interest, but is beyond the scope of this paper. We note that lower-resolution PMIP experiments should be used with caution, as lower-resolution models are unlikely to properly capture the behavior of humidity (Sherwood et al., 2010).

5. Summary

In this study, we applied the GCM ECHAM5 to explore how precipitation seasonality changed across the TP and CA during the mid-Holocene, LGM, and mid-Pliocene compared to pre-industrial conditions. Our initial hypothesis that the change in WJ position, and the intensity, strength and duration of the EASM, the SASM, and the ISM would influence the precipitation seasonality and thus surface hydroclimate over the TP and CA regions during glacial/interglacial appears to be correct. The following points highlight the magnitude of change observed:

1. There is a shift in the LGM and mid-Pliocene seasonal cycle of precipitation across the TP and CA. The "rainy season" is prolonged in the mid-Pliocene (from April to October) and shortened in the LGM (from June to August). Mid-Holocene mean seasonal precipitation is similar to that of the pre-industrial.
2. Moisture transport is substantially increased in the westerlies domain for the mid-Pliocene, reduced for the LGM, and remains mostly unchanged in the mid-Holocene.
3. All paleoclimate simulations produce a seasonal migration of the WJ. In warm periods (e.g., mid-Pliocene or interglacial) the WJ migrates farther north, which coincides with increased regional precipitation over TP and CA. During cooler periods (e.g., LGM or glacial), the WJ remains over relatively low latitudes, resulting in a drier CA. Moreover, the seasonal transition of the WJ occurs earlier (later) in the year in mid-Pliocene (LGM)-like climates.
4. Precipitation over the TP and CA is positively correlated with the latitudinal position of the WJ, ISM, SASM, and EASM strength on an annual timescale.
5. The findings above ought to be considered in the interpretation of ice cores, in situ carbonate $\delta^{18}O$, pollen records, drying in CA, geomorphological evidence for lake levels and other paleoclimate proxy data.

Data Availability Statement

The ECHAM model is available under the conditions of the "MPI-M Software Licence Agreement", which must be signed by each user. The "MPI-M Software Licence Agreement" and the information on the distribution of MPI-M models are given on: https://mpimet.mpg.de/fileadmin/projekte/ICON-ESM/mpi-m_sla_201202.pdf. The code of the isotopic version ECHAM5-wiso is available upon request on the GitLab repository of the Alfred Wegener Institute (Germany): https://gitlab.awi.de/mwerner/mpi-esm-wiso. The ECHAM5-wiso model output data (Botsyun et al., 2021) used in this study in netcdf format are available at https://zenodo.org/record/5445610.

Acknowledgments
We thank two anonymous reviewers for their helpful and constructive comments. This study was funded by the German Ministry for Education and Research (BMBF) as a part of the program "Central Asia - Monsoon Dynamics and Geo-Ecosystems II" (CAME II) within Q-TiP project "Quaternary Tipping Points of Lake Systems in the Arid Zone of Central Asia" (03G08063 C and 03G08063 A to D.E.S. and to T.A.E., respectively). This work used resources of the Deutsches Klimarechenzentrum (DKRZ) granted by its Scientific Steering Committee (WLA) under project bb1023, and of the University of Tübingen research cluster. Open Access funding enabled and organized by Projekt DEAL.

References

Abe-Ouchi, A., Saito, F., Kageyama, M., Braconnot, P., Harrison, S. P., Lambeck, K., et al. (2015). Ice-sheet configuration in the CMIP5/PMIP3 Last Glacial Maximum experiments. *Geoscientific Model Development*, *8*, 3621–3637. https://doi.org/10.5194/gmd-8-3621-2015

Abhik, S., Mukhopadhyay, P., & Goswami, B. N. (2014). Evaluation of mean and intraseasonal variability of Indian summer monsoon simulation in ECHAM5: Identification of possible source of bias. *Climate Dynamics*, *43*, 389–406. https://doi.org/10.1007/s00382-013-1824-7

An, Z., Colman, S. M., Zhou, W., Li, X., Brown, E. T., Jull, A. J. T., et al. (2012). Interplay between the Westerlies and Asian monsoon recorded in Lake Qinghai sediments since 32 ka. *Scientific Reports*, *2*, 619. https://doi.org/10.1038/srep00619

Ao, H., Rohling, E. J., Zhang, R., Roberts, A. P., Holbourn, A. E., Ladant, J.-B., et al. (2021). Global warming-induced Asian hydrological climate transition across the Miocene–Pliocene boundary. *Nature Communications*, *12*, 6935. https://doi.org/10.1038/s41467-021-27054-5

Argyilan, E. P., & Forman, S. L. (2003). Lake level response to seasonal climatic variability in the Lake Michigan-Huron system from 1920 to 1995. *Journal of Great Lakes Research*, *29*, 488–500. https://doi.org/10.1016/s0380-1330(03)70453-5

Arnold, L., Bréon, F.-M., & Brewer, S. (2009). The Earth as an extrasolar planet: The vegetation spectral signature today and during the last quaternary climatic extrema. *International Journal of Astrobiology*, *8*, 81–94. https://doi.org/10.1017/s1473550409004406

Baldwin, J., & Vecchi, G. (2016). Influence of the Tian Shan mountains on arid extratropical Asia. *Journal of Climate*, *29*(16), 5741–5762. https://doi.org/10.1175/JCLI-D-15-0490.1

Bigelow, N. H., Brubaker, L. B., Edwards, M. E., Harrison, S. P., Prentice, I. C., Anderson, P. M., et al. (2003). Climate change and Arctic ecosystems: 1. Vegetation changes north of 55° N between the Last Glacial Maximum, mid-Holocene, and present. *Journal of Geophysical Research*, *108*, 8170. https://doi.org/10.1029/2002jd002558

Bohner, J. (2006). General climatic controls and topoclimatic variations in Central and High Asia. *Boreas*, *35*, 279–295. https://doi.org/10.1080/03009480500456073

Bothe, O., Fraedrich, K., & Zhu, X. (2011). Large-scale circulations and Tibetan Plateau summer drought and wetness in a high-resolution climate model. *International Journal of Climatology*, *31*, 832–846. https://doi.org/10.1002/joc.2124

Bothe, O., Fraedrich, K., & Zhu, X. (2012). Precipitation climate of Central Asia and the large-scale atmospheric circulation. *Theoretical and Applied Climatology*, *108*, 345–354. https://doi.org/10.1007/s00704-011-0537-2

Botsyun, S., & Ehlers, T. A. (2021). How can climate models be used in paleoelevation reconstructions? *Frontiers of Earth Science*, *9*, 28. https://doi.org/10.3389/feart.2021.624542

Botsyun, S., Ehlers, T. A., Mutz, S. G., Methner, K., Krsnik, E., & Mulch, A. (2020). Opportunities and challenges for paleoaltimetry in "small" orogens: Insights from the European Alps. *Geophysical Research Letters*, *47*, e2019GL086046. https://doi.org/10.1029/2019GL086046

Botsyun, S., Mutz, S. G., Ehlers, T. A., Koptev, A., Wang, X., Schmidt, B., et al. (2021). Hydroclimate of the Tibetan Plateau and Central Asia during the Late Cenozoic [data set]. Zenodo. https://zenodo.org/record/5445610

Botsyun, S., Sepulchre, P., Donnadieu, Y., Risi, C., Licht, A., & Caves Rugenstein, J. K. (2019). Revised paleoaltimetry data show low Tibetan Plateau elevation during the Eocene. *Science*, *363*(80), eaaq1436. https://doi.org/10.1126/science.aaq1436

Botsyun, S., Sepulchre, P., Risi, C., & Donnadieu, Y. (2016). Impacts of Tibetan Plateau uplift on atmospheric dynamics and associated precipitation $\delta^{18}O$. *Climate of the Past*, *12*, 1401–1420. https://doi.org/10.5194/cp-12-1401-2016

Braconnot, P., Otto-Bliesner, B., Harrison, S., Joussaume, S., Peterchmitt, J.-Y., Abe-Ouchi, A., et al. (2007). Results of PMIP2 coupled simulations of the mid-Holocene and Last Glacial Maximum–Part 1: Experiments and large-scale features. *Climate of the Past*, *3*, 261–277. https://doi.org/10.5194/cp-3-261-2007

Broccoli, A. J., & Manabe, S. (1992). The effects of orography on midlatitude Northern Hemisphere dry climates. *Journal of Climate*, *5*(11), 1181–1201. https://doi.org/10.1175/1520-0442(1992)005<1181:teooom>2.0.co;2

Caves, J. K., Sjostrom, D. J., Mix, H. T., Winnick, M. J., & Chamberlain, C. P. (2014). Aridification of central Asia and uplift of the Altai and Hangay mountains, Mongolia: Stable isotope evidence. *American Journal of Science*, *314*, 1171–1201. https://doi.org/10.2475/08.2014.01

Caves Rugenstein, J. K., & Chamberlain, C. P. (2018). The evolution of hydroclimate in Asia over the Cenozoic: A stable-isotope perspective. *Earth-Science Reviews*, *185*, 1129–1156. https://doi.org/10.1016/j.earscirev.2018.09.003

Chang, C. P., Harr, P., & Ju, J. (2001). Possible roles of Atlantic circulations on the weakening Indian monsoon rainfall–ENSO relationship. *Journal of Climate*, *14*, 2376–2380. https://doi.org/10.1175/1520-0442(2001)014<2376:proaco>2.0.co;2

Chen, F., Yu, Z., Yang, M., Ito, E., Wang, S., Madsen, D. B., et al. (2008). Holocene moisture evolution in arid central Asia and its out-of-phase relationship with Asian monsoon history. *Quaternary Science Reviews*, *27*, 351–364. https://doi.org/10.1016/j.quascirev.2007.10.017

Chen, Y., Zong, Y., Li, B., Li, S., & Aitchison, J. C. (2013). Shrinking lakes in Tibet linked to the weakening Asian monsoon in the past 8.2 ka. *Quaternary Research*, *80*, 189–198. https://doi.org/10.1016/j.yqres.2013.06.008

Cheng, H., Zhang, P. Z., Spötl, C., Edwards, R. L., Cai, Y. J., Zhang, D. Z., et al. (2012). The climatic cyclicity in semiarid-arid central Asia over the past 500,000 years. *Geophysical Research Letters*, *39*, L01705. https://doi.org/10.1029/2011GL050202

Chiang, J. C. H., Herman, M. J., Yoshimura, K., & Fung, I. Y. (2020). Enriched East Asian oxygen isotope of precipitation indicates reduced summer seasonality in regional climate and westerlies. *Proceedings of National Academy of Sciences*, *117*, 14745–14750. https://doi.org/10.1073/pnas.1922602117

CLIMAP Project. (1981). *Seasonal reconstructions of the Earth's surface at the Last Glacial Maximum*. Geological Society of America.

Coumou, D., Lehmann, J., & Beckmann, J. (2015). The weakening summer circulation in the Northern Hemisphere mid-latitudes. *S*cience, *348*(80), 324–327. https://doi.org/10.1126/science.1261768

Dettman, D. L., Kohn, M. J., Quade, J., Ryerson, F. J., Ojha, T. P., & Hamidullah, S. (2001). Seasonal stable isotope evidence for a strong Asian monsoon throughout the past 10.7 m.y. *Geology*, *29*, 31–34. https://doi.org/10.1130/0091-7613(2001)029<0031:ssiefa>2.0.co;2.CO;2

Dietrich, S., Werner, M., Spangehl, T., & Lohmann, G. (2013). Influence of orbital forcing and solar activity on water isotopes in precipitation during the mid- and late Holocene. *Climate of the Past*, *9*, 13–26. https://doi.org/10.5194/cp-9-13-2013

Ding, Q., & Wang, B. (2005). Circumglobal teleconnection in the Northern Hemisphere summer. *Journal of Climate*, *18*, 3483–3505. https://doi.org/10.1175/jcli3473.1

Dowsett, H., Robinson, M., Haywood, A. M., Salzmann, U., Hill, D., Sohl, L. E., et al. (2010). The PRISM3D paleoenvironmental reconstruction. *Stratigraphy*, *7*, 123–139.

Du, Y., Li, T., Xie, Z., & Zhu, Z. (2016). Interannual variability of the Asian subtropical westerly jet in boreal summer and associated with circulation and SST anomalies. *Climate Dynamics*, *46*, 2673–2688. https://doi.org/10.1007/s00382-015-2723-x

Dugam, S. S., Kakade, S. B., & Verma, R. K. (1997). Interannual and long-term variability in the North Atlantic Oscillation and Indian summer monsoon rainfall. *Theoretical and Applied Climatology*, *58*, 21–29. https://doi.org/10.1007/bf00867429

Etheridge, D. M., Steele, L., Francey, R. J., & Langenfelds, R. L. (1998). Atmospheric methane between 1000 AD and present: Evidence of anthropogenic emissions and climatic variability. *Journal of Geophysical Research*, *103*, 15979–15993. https://doi.org/10.1029/98jd00923

Etheridge, D. M., Steele, L. P., Langenfelds, R. L., Francey, R. J., Barnola, J., & Morgan, V. I. (1996). Natural and anthropogenic changes in atmospheric CO_2 over the last 1000 years from air in Antarctic ice and firn. *Journal of Geophysical Research*, *101*, 4115–4128. https://doi.org/10.1029/95jd03410

Fang, X., An, Z., Clemens, S. C., Zan, J., Shi, Z., Yang, S., & Han, W. (2020). The 3.6-Ma aridity and westerlies history over midlatitude Asia linked with global climatic cooling. *Proceedings of National Academy of Sciences*, *117*, 24729–24734. https://doi.org/10.1073/pnas.1922710117

Fasullo, J., & Webster, P. J. (2003). A hydrological definition of Indian Monsoon onset and withdrawal. *Journal of Climate*, *16*, 3200–3211. https://doi.org/10.1175/1520-0442(2003)016<3200a:ahdoim>2.0.co;2

Fujita, K. (2008). Effect of precipitation seasonality on climatic sensitivity of glacier mass balance. *Earth and Planetary Science Letters*, *276*, 14–19. https://doi.org/10.1016/j.epsl.2008.08.028

Gildor, H., & Ghil, M. (2002). Phase relations between climate proxy records: Potential effect of seasonal precipitation changes. *Geophysical Research Letters*, *29*, 11. https://doi.org/10.1029/2001gl013781

Giner, M. M., García, J. S. C., & Sellés, J. G. (1999). Aerobiology of Artemisia airborne pollen in Murcia (SE Spain) and its relationship with weather variables: Annual and intradiurnal variations for three different species. Wind vectors as a tool in determining pollen origin. *International Journal of Biometeorology*, *43*, 51–63. https://doi.org/10.1007/s004840050116

Gong, D., & Ho, C. (2003). Arctic oscillation signals in the East Asian summer monsoon. *Journal of Geophysical Research*, *108*, 4066. https://doi.org/10.1029/2002jd002193

Haese, B., Werner, M., & Lohmann, G. (2013). Stable water isotopes in the coupled atmosphere-land surface model ECHAM5-J*SBACH*. *Geoscientific Model Development*, *6*, 1463–1480. https://doi.org/10.5194/gmd-6-1463-2013

Hagemann, S. (2002*). An improved land surface parameter dataset for global and regional climate mod*els. Report/Max–Plank–Institut für Meteorologie, 336.

Han, W., Appel, E., Galy, A., Rösler, W., Fang, X., Zhu, X., et al. (2020). Climate transition in the Asia inland at 0.8–0.6 Ma related to astronomically forced ice sheet expansion. *Quaternary Science Reviews*, *248*, 106580. https://doi.org/10.1016/j.quascirev.2020.106580

Han, W., Fang, X., Ye, C., Teng, X., & Zhang, T. (2014). Tibet forcing quaternary stepwise enhancement of westerly jet and central Asian aridification: Carbonate isotope records from deep drilling in the Qaidam salt playa, NE Tibet. *Global and Planetary Change*, *116*, 68–75. https://doi.org/10.1016/j.gloplacha.2014.02.006

Han, Z., Zhang, Q., Li, Q., Feng, R., Haywood, A. M., Tindall, J. C., et al. (2021). Evaluating the large-scale hydrological cycle response within the Pliocene Model Intercomparison Project Phase 2 (PlioMIP2) ensemble. *Climate of the Past*, *17*, 2537–2558. https://doi.org/10.5194/cp-17-2537-2021

Harrison, S. P., Yu, G., Takahara, H., & Prentice, I. C. (2001). Diversity of temperate plants in East Asia. *Nature*, *413*, 129–130. https://doi.org/10.1038/35093166

Haywood, A. M., Dowsett, H. J., Dolan, A. M., Rowley, D., Abe-Ouchi, A., Otto-Bliesner, B., et al. (2016). The Pliocene Model Intercomparison Project (PlioMIP) Phase 2: Scientific objectives and experimental design. *Climate of the Past*, *12*, 663–675. https://doi.org/10.5194/cp-12-663-2016

Haywood, A. M., Dowsett, H. J., Otto-Bliesner, B., Chandler, M. A., Dolan, A. M., Hill, D. J., et al. (2010). Pliocene Model Intercomparison Project (PlioMIP): Experimental design and boundary conditions (experiment 1). *Geoscientific Model Development*, *3*, 227–242. https://doi.org/10.5194/gmd-3-227-2010

Haywood, A. M., Hill, D. J., Dolan, A. M., Otto-Bliesner, B. L., Bragg, F., Chan, W. L., et al. (2013). Large-scale features of Pliocene climate: Results from the Pliocene Model Intercomparison Project. *Climate of the Past*, *9*, 191–209. https://doi.org/10.5194/cp-9-191-2013

He, C., Liu, Z., Otto-Bliesner, B. L., Brady, E. C., Zhu, C., Tomas, R., et al. (2021). Hydroclimate footprint of pan-Asian monsoon water isotope during the last deglaciation. *Science Advances*, *7*, eabe2611. https://doi.org/10.1126/sciadv.abe2611

Herzschuh, U., Cao, X., Laepple, T., Dallmeyer, A., Telford, R. J., Ni, J., et al. (2019). Position and orientation of the westerly jet determined Holocene rainfall patterns in China. *Nature Communications*, *10*, 2376. https://doi.org/10.1038/s41467-019-09866-8

Hoskins, B. (1996). On the existence and strength of the summer subtropical anticyclones: Bernhard Haurwitz memorial lecture. *Bulletin of the American Meteorological Society*, *77*, 1287–1292.

Hurrell, J. W. (1995). Decadal trends in the north Atlantic oscillation: Regional temperatures and precipitation. *Science*, *269*(80), 676–679. https://doi.org/10.1126/science.269.5224.676

Hurrell, J. W. (1996). Influence of variations in extratropical wintertime teleconnections on Northern Hemisphere temperature. *Geophysical Research Letters*, *23*, 665–668. https://doi.org/10.1029/96gl00459

Jiang, J., Zhou, T., Wang, H., Qian, Y., Noone, D., & Man, W. (2020). Tracking moisture sources of precipitation over central Asia: A study based on the water-source-tagging method. *Journal of Climate*, *33*, 10339–10355. https://doi.org/10.1175/JCLI-D-20-0169.1

Jin, L., Chen, F., Morrill, C., Otto-Bliesner, B. L., & Rosenbloom, N. (2012). Causes of early Holocene desertification in arid central Asia. *Climate Dynamics*, *38*, 1577–1591. https://doi.org/10.1007/s00382-011-1086-1

Joshi, M. M., Gregory, J. M., Webb, M. J., Sexton, D. M. H., & Johns, T. C. (2008). Mechanisms for the land/sea warming contrast exhibited by simulations of climate change. *Climate Dynamics*, *30*, 455–465. https://doi.org/10.1007/s00382-007-0306-1

Kamae, Y., Yoshida, K., & Ueda, H. (2016). Sensitivity of Pliocene climate simulations in MRI-CGCM2. 3 to respective boundary conditions. *Climate of the Past*, *12*, 1619–1634. https://doi.org/10.5194/cp-12-1619-2016

Kapp, P., Pelletier, J. D., Rohrmann, A., Heermance, R., Russell, J., & Ding, L. (2011). Wind erosion in the Qaidam basin, central Asia: Implications for tectonics, paleoclimate, and the source of the Loess Plateau. *Geological Society of America Today*, *21*, 4–10. https://doi.org/10.1130/GSATG99A.1

Kendon, E. J., Ban, N., Roberts, N. M., Fowler, H. J., Roberts, M. J., Chan, S. C., et al. (2017). Do convection-permitting regional climate models improve projections of future precipitation change? *Bulletin of American Meteorological Society*, *98*, 79–93. https://doi.org/10.1175/BAMS-D-15-0004.1

Knorr, G., Butzin, M., Micheels, A., & Lohmann, G. (2011). A warm Miocene climate at low atmospheric CO2 levels. *Geophysical Research Letters*, *38*, L20701. https://doi.org/10.1029/2011gl048873

Krishnan, R., Kumar, V., Sugi, M., & Yoshimura, J. (2009). Internal feedbacks from monsoon-midlatitude interactions during droughts in the Indian summer monsoon. *Journal of the Atmospheric Sciences*, *66*, 553–578. https://doi.org/10.1175/2008JAS2723.1

Lei, Y., Yao, T., Yang, K., Sheng, Y., Kleinherenbrink, M., Yi, S., et al. (2017). Lake seasonality across the Tibetan Plateau and their varying relationship with regional mass changes and local hydrology. *Geophysical Research Letters*, *44*, 892–900. https://doi.org/10.1002/2016gl072062

Li, J., Ehlers, T. A., Mutz, S. G., Steger, C., Paeth, H., Werner, M., et al. (2016). Modern precipitation $\delta^{18}O$ and trajectory analysis over the Himalaya-Tibet orogen from ECHAM5-wiso simulations: Tibetan modern precipitation δ 18 O. *Journal of Geophysical Research: Atmospheres*, *121*, 10410–10452. https://doi.org/10.1002/2016JD024818

Li, J., Ehlers, T. A., Werner, M., Mutz, S. G., Steger, C., & Paeth, H. (2016). Late quaternary climate, precipitation $\delta^{18}O$, and Indian monsoon variations over the Tibetan Plateau. *Earth and Planetary Science Letters*, *457*, 412–422. https://doi.org/10.1016/j.epsl.2016.09.031

Li, J., Yu, R., & Zhou, T. (2008). Teleconnection between NAO and climate downstream of the Tibetan Plateau. *Journal of Climate*, *21*, 4680–4690. https://doi.org/10.1175/2008jcli2053.1

Li, J., & Zeng, Q. (2002). A unified monsoon index. *Geophysical Research Letters*, *29*, 1151–1154. https://doi.org/10.1029/2001gl013874

Li, W., Li, L., Ting, M., & Liu, Y. (2012). Intensification of Northern Hemisphere subtropical highs in a warming climate. *Nature Geoscience*, *5*, 830–834. https://doi.org/10.1038/ngeo1590

Li, Y., & Morrill, C. (2010). Multiple factors causing Holocene lake-level change in monsoonal and arid central Asia as identified by model experiments. *Climate Dynamics*, *35*, 1115–1132. https://doi.org/10.1007/s00382-010-0861-8

Li, Y., & Morrill, C. (2013). Lake levels in Asia at the Last Glacial Maximum as indicators of hydrologic sensitivity to greenhouse gas concentrations. *Quaternary Science Reviews*, *60*, 1–12. https://doi.org/10.1016/j.quascirev.2012.10.045

Licht, A., Van Cappelle, M., Abels, H. A., Ladant, J.-B., Trabucho-Alexandre, J., France-Lanord, C., et al. (2014). Asian monsoons in a late Eocene greenhouse world. *Nature*, *513*, 501–506. https://doi.org/10.1038/nature13704

Löfverström, M., Caballero, R., Nilsson, J., & Messori, G. (2016). Stationary wave reflection as a mechanism for zonalizing the Atlantic winter jet at the LGM. *Journal of the Atmospheric Sciences*, *73*, 3329–3342. https://doi.org/10.1175/JAS-D-15-0295.1

Lohmann, G., Pfeiffer, M., Laepple, T., Leduc, G., & Kim, J.-H. (2013). A model–data comparison of the Holocene global sea surface temperature evolution. *Climate of the Past*, *9*, 1807–1839. https://doi.org/10.5194/cp-9-1807-2013

Lorenz, S. J., & Lohmann, G. (2004). Acceleration technique for Milankovitch type forcing in a coupled atmosphere-ocean circulation model: Method and application for the Holocene. *Climate Dynamics*, *23*, 727–743. https://doi.org/10.1007/s00382-004-0469-y

Lü, J. M., Kim, S. J., Abe-Ouchi, A., Yu, Y., & Ohgaito, R. (2010). Arctic oscillation during the mid-Holocene and Last Glacial Maximum from PMIP2 coupled model simulations. *Journal of Climate*, *23*, 3792–3813. https://doi.org/10.1175/2010JCLI3331.1

Ma, Y., Lu, M., Chen, H., Pan, M., & Hong, Y. (2018). Atmospheric moisture transport versus precipitation across the Tibetan plateau: A mini-review and current challenges. *Atmospheric Research*, *209*, 50–58. https://doi.org/10.1016/j.atmosres.2018.03.015

Maussion, F., Scherer, D., Mölg, T., Collier, E., Curio, J., & Finkelnburg, R. (2014). Precipitation seasonality and variability over the Tibetan Plateau as resolved by the High Asia Reanalysis. *Journal of Climate*, *27*, 1910–1927. https://doi.org/10.1175/JCLI-D-13-00282.1

Meehl, G. A., Covey, C., Taylor, K. E., Delworth, T., Stouffer, R. J., Latif, M., et al. (2007). The WCRP CMIP3 multimodel dataset: A new era in climate change research. *Bulletin of American Meteorological Society*, *88*, 1383–1394. https://doi.org/10.1175/bams-88-9-1383

Miao, Y., Fang, X., Liu, Y.-S. C., Yan, X., Li, S., & Xia, W. (2016). Late Cenozoic pollen concentration in the Western Qaidam Basin, northern Tibetan Plateau, and its significance for paleoclimate and tectonics. *Review of Palaeobotany and Palynology*, *231*, 14–22. https://doi.org/10.1016/j.revpalbo.2016.04.008

Mölg, T., Maussion, F., Collier, E., Chiang, J. C. H., & Scherer, D. (2017). Prominent midlatitude circulation signature in High Asia's surface climate during monsoon. *Journal of Geophysical Research: Atmospheres*, *122*, 12702–12712. https://doi.org/10.1002/2017JD027414

Mölg, T., Maussion, F., & Scherer, D. (2014). Mid-latitude westerlies as a driver of glacier variability in monsoonal High Asia. *Nature Climate Change*, *4*, 68–73. https://doi.org/10.1038/nclimate2055

Mölg, T., Maussion, F., Yang, W., & Scherer, D. (2012). The footprint of Asian monsoon dynamics in the mass and energy balance of a Tibetan glacier. *Cryosphere*, *6*, 1445–1461. https://doi.org/10.5194/tc-6-1445-2012

Mutz, S. G., Ehlers, T. A., Werner, M., Lohmann, G., Stepanek, C., & Li, J. (2018). Estimates of late Cenozoic climate change relevant to Earth surface processes in tectonically active orogens. *Earth Surface Dynamics*, *6*, 271–301. https://doi.org/10.5194/esurf-6-271-2018

Otto-Bliesner, B. L., Brady, E. C., Clauzet, G., Tomas, R., Levis, S., & Kothavala, Z. (2006). Last Glacial Maximum and Holocene climate in CCSM3. *Journal of Climate*, *19*, 2526–2544. https://doi.org/10.1175/jcli3748.1

Pan, C., Zhu, B., Gao, J., Kang, H., & Zhu, T. (2019). Quantitative identification of moisture sources over the Tibetan Plateau and the relationship between thermal forcing and moisture transport. *Climate Dynamics*, *52*, 181–196. https://doi.org/10.1007/s00382-018-4130-6

Pausata, F. S. R., Li, C., Wettstein, J. J., Nisancioglu, K. H., & Battisti, D. S. (2009). Changes in atmospheric variability in a glacial climate and the impacts on proxy data: A model intercomparison. *Climate of the Past*, *5*, 489–502. https://doi.org/10.5194/cp-5-489-2009

Pickett, E. J., Harrison, S. P., Hope, G., Harle, K., Dodson, J. R., Peter Kershaw, A., et al. (2004). Pollen-based reconstructions of biome distributions for Australia, Southeast Asia and the Pacific (SEAPAC region) at 0, 6000 and 18,000 14C yr BP. *Journal of Biogeography*, *31*, 1381–1444. https://doi.org/10.1111/j.1365-2699.2004.01001.x

Prasad, V. S., & Hayashi, T. (2007). Active, weak and break spells in the Indian summer monsoon. *Meteorology and Atmospheric Physics*, *95*, 53–61. https://doi.org/10.1007/s00703-006-0197-4

Prentice, I. C., Jolly, D., & Participants, B. (2000). Mid-Holocene and glacial-maximum vegetation geography of the northern continents and Africa. *Journal of Biogeography*, *27*, 507–519.

Rajeevan, M. (2002). Winter surface pressure anomalies over Eurasia and Indian summer monsoon. *Geophysical Research Letters*, *29*, 91–94. https://doi.org/10.1029/2001gl014363

Roeckner, E., Bäuml, G., Bonaventura, L., Brokopf, R., Esch, M., Giorgetta, M., et al. (2003). *The atmospheric general circulation model ECHAM 5. PART I: Model description*. Report/Max–Plank–Institute für Meteorologie, 349.

Ronay, E. R., Breitenbach, S. F. M., & Oster, J. L. (2019). Sensitivity of speleothem records in the Indian Summer Monsoon region to dry season infiltration. *Scientific Reports*, *9*, 5091. https://doi.org/10.1038/s41598-019-41630-2

Saeed, S., Müller, W. A., Hagemann, S., & Jacob, D. (2011). Circumglobal wave train and the summer monsoon over northwestern India and Pakistan: The explicit role of the surface heat low. *Climate Dynamics*, *37*, 1045–1060. https://doi.org/10.1007/s00382-010-0888-x

Sampe, T., & Xie, S. P. (2010). Large-scale dynamics of the meiyu-baiu rainband: Environmental forcing by the westerly jet. *Journal of Climate*, *23*, 113–134. https://doi.org/10.1175/2009JCLI3128.1

Sarnthein, M., Gersonde, R., Niebler, S., Pflaumann, U., Spielhagen, R., Thiede, J., et al. (2003). Overview of glacial Atlantic Ocean mapping (GLAMAP 2000). *Paleoceanography*, *18*, 1030. https://doi.org/10.1029/2002pa000769

Schäfer-Neth, C., & Paul, A. (2003). The Atlantic Ocean at the Last Glacial Maximum: 1. Objective mapping of the GLAMAP sea-surface conditions. In G. Wefer, S. Mulitza, & V. Ratmeyer (Eds.), *The South Atlantic in the late quaternary*. Springer. https://doi.org/10.1007/978-3-642-18917-3_23

Scherer, D. (2020). Survival of the Qaidam mega-lake system under mid-Pliocene climates and its restoration under future climates. *Hydrology and Earth System Sciences*, *24*, 3835–3850. https://doi.org/10.5194/hess-24-3835-2020

Schiemann, R., Lüthi, D., & Schär, C. (2009). Seasonality and interannual variability of the westerly jet in the Tibetan Plateau region. *Journal of Climate*, *22*, 2940–2957. https://doi.org/10.1175/2008jcli2625.1

Sherwood, S. C., Ingram, W., Tsushima, Y., Satoh, M., Roberts, M., Vidale, P. L., & O'Gorman, P. A. (2010). Relative humidity changes in a warmer climate. *Journal of Geophysical Research*, *115*, D09104. https://doi.org/10.1029/2009jd012585

Sohl, L. E., Chandler, M. A., Schmunk, R. B., Mankoff, K., Jonas, J. A., Foley, K. M., & Dowsett, H. J. (2009). PRISM3/GISS topographic reconstruction. *US Geological Survey Data Series*, *419*. https://doi.org/10.3133/ds419

Sowers, T., Alley, R. B., & Jubenville, J. (2003). Ice core records of atmospheric N2O covering the last 106,000 years. *Science*, *301*(5635), 945–948. https://doi.org/10.1126/science.1085293

Stauch, G. (2015). Geomorphological and palaeoclimate dynamics recorded by the formation of aeolian archives on the Tibetan Plateau. *Earth-Science Reviews*, *150*, 393–408. https://doi.org/10.1016/j.earscirev.2015.08.009

Stepanek, C., & Lohmann, G. (2012). Modelling mid-Pliocene climate with COSMOS. *Geoscientific Model Development*, *5*, 1221–1243. https://doi.org/10.5194/gmd-5-1221-2012

Sun, Y., Ramstein, G., Contoux, C., & Zhou, T. (2013). A comparative study of large-scale atmospheric circulation in the context of a future scenario (RCP4. 5) and past warmth (mid-Pliocene). *Climate of the Past*, *9*, 1613–1627. https://doi.org/10.5194/cp-9-1613-2013

Sun, Y., Wu, H., Kageyama, M., Ramstein, G., Li, L. Z. X., Tan, N., et al. (2021). The contrasting effects of thermodynamic and dynamic processes on East Asian summer monsoon precipitation during the Last Glacial Maximum: A data-model comparison. *Climate Dynamics*, *56*, 1303–1316. https://doi.org/10.1007/s00382-020-05533-7

Sun, Y., Wu, H., Ramstein, G., Liu, B., Zhao, Y., Li, L., et al. (2021). *Revisiting the physical mechanisms of east Asian summer monsoon precipitation changes during the mid-holocene: A data–model comparison*. Research Square. https://doi.org/10.21203/rs.3.rs-390166/v1

Tan, N., Contoux, C., Ramstein, G., Sun, Y., Dumas, C., & Sepulchre, P. (2020). Modelling a modern-like pCO_2 warm period (Marine Isotope Stage KM5c) with two versions of an Instatute Pierre Simon Laplace atmosphere-ocean coupled general circulation model. *Climate of the Past*, *16*, 1–16. https://doi.org/10.5194/cp-16-1-2020

Tang, L., Shen, C., Liu, K., & Overpeck, J. T. (2000). Changes in south Asian monsoon: New high-resolution paleoclimatic records from Tibet, China. *Chinese Science Bulletin*, *45*, 87–91. https://doi.org/10.1007/bf02884911

Toggweiler, J. R., & Russell, J. (2008). Ocean circulation in a warming climate. *Nature*, *451*, 286–288. https://doi.org/10.1038/nature06590

Tselioudis, G., Douvis, C., & Zerefos, C. (2012). Does dynamical downscaling introduce novel information in climate model simulations of precipitation change over a complex topography region? *International Journal of Climatology*, *32*, 1572–1578. https://doi.org/10.1002/joc.2360

Wang, B., Clemens, S. C., & Liu, P. (2003). Contrasting the Indian and East Asian monsoons: Implications on geologic timescales. *Marine Geology*, *201*, 5–21. https://doi.org/10.1016/S0025-3227(03)00196-8

Wang, H. (2002). The instability of the east Asian summer monsoon-ENSO relations. *Advances in Atmospheric Sciences*, *19*, 1–11. https://doi.org/10.1007/s00376-002-0029-5

Wang, H., Lu, H., Zhao, L., Zhang, H., Lei, F., & Wang, Y. (2019). Asian monsoon rainfall variation during the Pliocene forced by global temperature change. *Nature Communications*, *10*, 1–8. https://doi.org/10.1038/s41467-019-13338-4

Wang, J.-H., Yin, A., Harrison, T. M., Grove, M., Zhang, Y.-Q., & Xie, G.-H. (2001). A tectonic model for Cenozoic igneous activities in the eastern Indo–Asian collision zone. *Earth and Planetary Science Letters*, *188*, 123–133. https://doi.org/10.1016/s0012-821x(01)00315-6

Wang, X., Schmidt, B., Otto, M., Ehlers, T. A., Mutz, S. G., Botsyun, S., & Scherer, D. (2021). Sensitivity of water balance in the Qaidam Basin to the mid-Pliocene climate. *Journal of Geophysical Research: Atmospheres*, *126*, e2020JD033965. https://doi.org/10.1029/2020jd033965

Wang, X., Tolksdorf, V., Otto, M., & Scherer, D. (2021). WRF-based dynamical downscaling of ERA5 reanalysis data for High Mountain Asia: Towards a new version of the High Asia Refined analysis. *International Journal of Climatology*, *41*, 743–762. https://doi.org/10.1002/joc.6686

Wang, Y., Lu, H., Wang, K., Wang, Y., Li, Y., Clemens, S., et al. (2020). Combined high-and low-latitude forcing of East Asian monsoon precipitation variability in the Pliocene warm period. *Science Advances*, *6*, eabc2414. https://doi.org/10.1126/sciadv.abc2414

Wei, W., & Lohmann, G. (2012). Simulated Atlantic multidecadal oscillation during the Holocene. *Journal of Climate*, *25*, 6989–7002. https://doi.org/10.1175/jcli-d-11-00667.1

Williams, G. P., & Bryan, K. (2006). Ice age winds: An aquaplanet model. *Journal of Climate*, *19*, 1706–1715. https://doi.org/10.1175/jcli3766.1

Wu, G., Liu, Y., Dong, B., Liang, X., Duan, A., Bao, Q., & Yu, J. (2012). Revisiting Asian monsoon formation and change associated with Tibetan plateau forcing: I. Formation. *Climate Dynamics*, *39*, 1169–1181. https://doi.org/10.1007/s00382-012-1334-z

Wu, Z., Li, J., Jiang, Z., He, J., & Zhu, X. (2012). Possible effects of the North Atlantic Oscillation on the strengthening relationship between the East Asian summer monsoon and ENSO. *International Journal of Climatology*, *32*, 794–800. https://doi.org/10.1002/joc.2309

Yang, S., Lau, K. M., Yoo, S. H., Kinter, J. L., Miyakoda, K., & Ho, C. H. (2004). Upstream subtropical signals preceding the Asian summer monsoon circulation. *Journal of Climate*, *17*, 4213–4229. https://doi.org/10.1175/jcli3192.1

Yao, T., Masson-Delmotte, V., Gao, J., Yu, W., Yang, X., Risi, C., et al. (2013). A review of climatic controls on $\delta^{18}O$ in precipitation over the Tibetan Plateau: Observations and simulations. *Reviews of Geophysics*, *51*, 525–548. https://doi.org/10.1002/rog.20023

Zhang, C., Zhang, W., Feng, Z., Mischke, S., Gao, X., Gao, D., & Sun, F. (2012). Holocene hydrological and climatic change on the northern Mongolian Plateau based on multi-proxy records from Lake Gun Nuur. *Palaeogeography, Palaeoclimatology, Palaeoecology*, *323–325*, 75–86. https://doi.org/10.1016/j.palaeo.2012.01.032

Zhang, H., Griffiths, M. L., Chiang, J. C. H., Kong, W., Wu, S., Atwood, A., et al. (2018). East Asian hydroclimate modulated by the position of the westerlies during Termination I. *Science*, *362*(80), 580–583. https://doi.org/10.1126/science.aat9393

Zhang, R., Jiang, D., Zhang, Z., Cheng, Z., & Zhang, Q. (2017). Comparison of the climate effects of surface uplifts from the northern Tibetan Plateau, the Tianshan, and the Mongolian Plateau on the East Asian climate. *Journal of Geophysical Research: Atmospheres*, *122*, 7949–7970. https://doi.org/10.1002/2017jd026470

Zhang, R., Jiang, D., Zhang, Z., Yan, Q., & Li, X. (2019). Modeling the late Pliocene global monsoon response to individual boundary conditions. *Climate Dynamics*, *53*, 4871–4886. https://doi.org/10.1007/s00382-019-04834-w

Zhao, J., An, C. B., Huang, Y., Morrill, C., & Chen, F. H. (2017). Contrasting early Holocene temperature variations between monsoonal East Asia and westerly dominated Central Asia. *Quaternary Science Reviews*, *178*, 14–23. https://doi.org/10.1016/j.quascirev.2017.10.036

Zhao, Y., Huang, A., Zhou, Y., Huang, D., Yang, Q., Ma, Y., et al. (2014). Impact of the middle and upper tropospheric cooling over central Asia on the summer rainfall in the Tarim Basin, China. *Journal of Climate*, *27*, 4721–4732. https://doi.org/10.1175/jcli-d-13-00456.1

Zhu, L., Lü, X., Wang, J., Peng, P., Kasper, T., Daut, G., et al. (2015). Climate change on the Tibetan Plateau in response to shifting atmospheric circulation since the LGM. *Scientific Reports*, *5*, 13318. https://doi.org/10.1038/srep13318